

DESIGN OF A MICROFLUIDIC DEVICE FOR LYMPHATIC BIOLOGY

A Thesis
Presented to
The Academic Faculty

by

Jamie L. Huffman

In Partial Fulfillment
of the Requirements for the Degree
Master of Science in Mechanical Engineering in the
School of Mechanical Engineering

Georgia Institute of Technology
December 2011

DESIGN OF A MICROFLUIDIC DEVICE FOR LYMPHATIC BIOLOGY

Approved by:

Professor J. Brandon Dixon, Advisor
School of Mechanical Engineering
Georgia Institute of Technology

Professor David Ku
School of Mechanical Engineering
Georgia Institute of Technology

Professor Craig Forest
School of Mechanical Engineering
Georgia Institute of Technology

Date Approved: 11 November 2011

*To my parents,
for always believing in me.*

ACKNOWLEDGEMENTS

I would like to thank the Dixon lab for all of their support throughout my entire project. Their encouragement, advice, and help are greatly appreciated. I'm thankful to Dr. Nipper for his excellent image processing lesson, Tyler O'Malley for his cancer expertise, and I am also especially thankful to Dr. Dixon whose great ideas and enthusiasm were particularly useful. Finally, I would like to thank the NIH for providing the funding for this project.

TABLE OF CONTENTS

DEDICATION	iii
ACKNOWLEDGEMENTS	iv
LIST OF TABLES	viii
LIST OF FIGURES	ix
SUMMARY	xi
I INTRODUCTION	1
1.1 Problem Statement	1
1.2 Solution and Benefits	1
II BACKGROUND	3
2.1 Lymphatic System	3
2.1.1 Primary Role	3
2.1.2 Fluid Homeostasis	3
2.1.3 Permeability	4
2.1.4 Immune Cell Trafficking	5
2.1.5 Lipid Transport	5
2.1.6 Lymphatic Dysfunction and Disease	6
2.2 Current Tissue-Engineered Models	7
2.2.1 Transwell Systems	7
2.2.2 Transwell System for Studying Lipid Transport	8
2.2.3 Cancer Metastasis	9
2.3 Importance of Flow	11
2.4 Variations of Current Tissue-Engineered Models	12
2.4.1 Lipid Transport	12
2.4.2 Cancer Metastasis	13
2.5 Project Requirements	14
2.5.1 Similar Devices	15

III METHODS	18
3.1 Design and Fabrication	18
3.1.1 Design Requirements	18
3.1.2 Manufacturing Requirements	20
3.1.3 Imaging	31
3.2 Device Preparation	36
3.2.1 PDMS	36
3.2.2 Plasma Treatment	36
3.3 Cell Culture	36
3.3.1 Lymphatic Endothelial Cells	36
3.3.2 Collagen Gel	37
3.3.3 Dextran/Bodipy Mix	38
3.3.4 Flow studies	38
3.4 Cell Staining	39
3.5 Image Processing	39
3.5.1 Permeability	39
3.5.2 Migration	40
IV RESULTS AND DISCUSSION	41
4.1 Aim 1: Cell Viability	41
4.2 Aim 2: Permeability	46
4.3 Aim 3: Migration	52
4.3.1 Interstitial Flow in Cancer Gel	52
4.3.2 Migration	54
V CONCLUSION	59
5.1 Conclusion	59
5.1.1 Future Work	59
APPENDIX A — MATLAB CODE	61
APPENDIX B — COMSOL SETUP IMAGES	71

REFERENCES 73

LIST OF TABLES

1	Fulfillment of Design Requirements by Prototype 1	20
2	Fulfillment of Design Requirements by Prototype 2	24
3	Fulfillment of Design Requirements by Prototype 3	27
4	Fulfillment of Design Requirements by Prototype 4	31
5	Fulfillment of Design Requirements by Modified Prototype 4	32
6	Images from final modification of prototype 4. 4 different dextran channels	35
7	Fulfillment of Design Requirements by Final Prototype 4	35
8	Flow increases effective permeability of Dextran	50
9	Flow increases effective permeability of Bodipy	51
10	Cell flux through collagen gel z slice	55

LIST OF FIGURES

1	Schematic of Cell Layers in Transwell System	8
2	Schematic of LEC Layer and Cancer Gel in Transwell System	9
3	Schematic of LEC Layer and Cancer Gel in Transwell System with Transmural Flow	10
4	Concentration Gradient of CCL19/21 Due to Presence of Flow	10
5	Flow through porous membrane with luminal flow and transmural flow present	13
6	Flow through collagen gel with cancer cells suspended in the gel	14
7	Lung on a chip cross sectional view and top view[1]	16
8	Schematic of flow channels with view of membrane layers[2]	17
9	Comsol rendering of flow in the bottom (left) and isometric (right) channels of prototype 1	19
10	Molds for bottom (left) and top (right) channels	22
11	Bridge for top mold	22
12	3D rendering of actual device (left) and top view (right)	23
13	Molds for bottom (left) and top (right) channels	24
14	Rendering of actual device	25
15	Molds for bottom (left) and top (right) channels	25
16	Molds for bottom (left) and top (right) channels	26
17	Rendering of modified prototype 3	26
18	Exploded view of the device (left) and clamped together view (right)	28
19	Cap (left) and middle (right) of stand	29
20	Mold for channels in prototype 4	29
21	Cross-sectional view of flow in prototype 4	30
22	PDMS channel cap (left) and mold (right)	30
23	Exploded view of final device and stand	32
24	Actual device with dyed channels	33

25	Assembly of membrane with slides and tubing connectors (left) with tube holder mold (right)	34
26	Final prototype with clamp and dyed channels	34
27	LECs stained with dapi and phalloidin	42
28	Co-culture of cancer cells with LECs	43
29	Co-culture with just dapi and rhodamine channels	44
30	Bright field image of cancer cells with live cell dye	45
31	LECs stained with dapi and phalloidin	46
32	LECs stained with dapi and phalloidin with bodipy deposits	46
33	Region of interest used in channels	48
34	Intensity vs Concentration for bodipy (left) and dextran (right)	48
35	Flow model with optically labeled tracer in bottom channel	49
36	Dextran permeability throughout experiment for static (left) and flow cases (right)	50
37	Bodipy permeability throughout experiment for static (left) and flow cases (right)	51
38	Initial height of media added to channel (left) and final height after 12 hours (right)	53
39	Side view of cross-sectional area (left) and isometric view of model (right)	53
40	Resulting image from subtraction	57
41	Magnitude and frequency of movement changes	58
42	Cancer cells suspended in collagen gel with luminal flow on LEC side	60
43	Boundary conditions	71
44	Subdomain conditions	72

SUMMARY

The lymphatic system has three primary roles: transporting lipids, transporting immune cells, and maintaining fluid balance. Each one of these roles are influenced by the presence of flow. Inflammation increases lymph flow, lipid uptake is enhanced by flow, cancer cell migration increases in the presence of flow, and lymphatic permeability and lymphatic contractility respond to changes in flow. Flow is very important to lymphatic function, and yet, there are no in vitro models that incorporate both luminal (flow along cell lumen) and transmural (flow through cell lumina) flow for lymphatics.

To address this need, a microfluidic device has been developed that can incorporate both of these types of flow. This is achieved by driving flow through a channel which creates a pressure gradient that drives fluid through a porous membrane into an adjacent channel. Following several design iterations, the device can be easily fabricated, imaged, and cells can grow and survive in it.

Permeability experiments have been performed in static and flow, 0.175 mL/min (0.5 dyne/cm²), cases. The effective permeability of dextran in the static and flow cases was calculated to be 0.0083 $\mu\text{m/s}$ and 2.05 $\mu\text{m/s}$ respectively. While the effective permeability of bodipy in the static and flow cases was calculated to be 0.0053 $\mu\text{m/s}$ and 2.57 $\mu\text{m/s}$ respectively. The static values are similar to values obtained in a transwell study by Dixon et al. As mentioned, lipid uptake is increased in the presence of flow and these numbers suggest the same.

In addition to permeability studies, experiments were performed with cancer cells suspended in a collagen gel. Two image processing techniques were used to quantify cancer cell migration. The first technique was used to calculate the number of cells

present at the beginning of the experiment and the number of cells that were ever present during the experiment in that particular z slice. The static case yielded a cell flux of 15 additional cells. While the two flow cases, within interstitial flow range, had a flux of 24 and 40 cells. This suggests that flow increases migration in cancer cells and is in agreement with the literature. The second technique was used to show that the cells in the static and flow cases are similarly motile, but the flow case is more directed in the z direction towards the membrane.

The future work for this device is quite extensive, but a strong foundation centered around basic capabilities like inducing flow, seeding cells, and imaging has been formed.

CHAPTER I

INTRODUCTION

1.1 Problem Statement

Lymphatics are responsible for transporting fluids, cells, and lipids [13] and, yet, very little is known about the molecular mechanisms involved in these tasks. Strides have been taken to develop tissue-engineered models that can be used to characterize the transport mechanisms involved [13], but these models do not account for transmural or luminal flow. Lymphatic function is immensely affected by interstitial flow [13][28][37][46][17], for example flow can act as a signaling cue to lymphatics during inflammation [37]. The lymphatics are also involved in cancer cell metastasis and transmural flow has been shown to act as a tumor cell homing mediator to lymphatics [52]. There are, however, no current models of lymphatics that can incorporate both luminal and transmural flow. A model that can better recapitulate the lymphatics would be an invaluable tool for studying the effects of flow on lymphatic endothelial cell function.

1.2 Solution and Benefits

A microfluidic device has been developed consisting of two channels that are separated by a porous membrane. This device is used in two specific disease models: a model of lymphedema and a model of cancer metastasis via lymphatics. Both luminal and transmural flow can be produced with this device. Luminal flow can be achieved by driving flow through a channel and over a cell layer. The act of driving this flow creates a pressure gradient through the porous membrane which results in transmural

flow going through the cell layer. Some benefits to using an in vitro model with three-dimensional microenvironments over an in vivo model include the use of human cells, polarization of transport, and separable inputs. In vitro experiments can be high throughput, quick and cost effective.

CHAPTER II

BACKGROUND

2.1 Lymphatic System

2.1.1 Primary Role

The lymphatic system is primarily responsible for maintaining fluid balance, transporting immune cells, and absorbing and delivering lipids to the circulatory system [13]. Without lymphatic function life stops [28]. There are two distinct types of lymphatic vessels: initial and collecting. The initial lymphatics are blind-ended tubes with “button-like” junctions [3]. When pressure gradients are present, these overlapping junctions allow for fluid to be driven into the lymphatics. Whereas, the collecting lymphatic junctions are more like “zippers” [3]. These junctions have much tighter interfaces and limit leaking. Overall, the initial lymphatics allow fluid to enter the lymphatic system and then the collecting lymphatics transport the lymph.

2.1.2 Fluid Homeostasis

In order to maintain normal tissue homeostasis, lymphatic vessels help to return the fluid or cells back into the circulatory system [65, 3] through the thoracic duct [15]. This process is also important in inflammatory diseases and cancer due to the high fluid and cell efflux [65, 3] into the tissue spaces that occurs in these conditions.

Both hydrostatic and colloidal osmotic pressure gradients facilitate entry into the collecting lymphatics [7, 49, 3], due to a disparity between the pressures [28]. Another important factor to consider is the permeability of the vessel wall which can change, because of the lymphatic’s dynamic nature [28]. Starling’s Law

$$J_v = L_P S(\Delta P - \sigma \Delta \pi) \tag{1}$$

takes these factors into consideration. Where J_v is the fluid flux across the surface area S , L_P is the hydraulic permeability, ΔP is the hydrostatic pressure, $\Delta\pi$ is the oncotic pressure, and σ is a non-dimensional coefficient of the effectiveness of the interface as a semi-permeable membrane [28]. This equation is generally used more often with collecting lymphatic vessels.

If the oncotic pressure in Starling's Law is greater than the hydrostatic pressure, then the flow can reverse in direction. Generally, in initial lymphatics the oncotic pressure is thought to be zero. Ficks' First Law

$$J_s = P_d \Delta C S \quad (2)$$

is used for initial lymphatics and it states that when a concentration gradient exists solutes will move in the direction of the gradient [28]. Where J_s is the solute fluid flux, P_d is the permeability, and ΔC is the concentration gradient [28].

2.1.3 Permeability

From equations 1 and 2 we can see that permeability plays a significant role in fluid homeostasis and permeability is not necessarily a constant value [27]. For example, depending on the health of the surrounding vessels and what signaling is occurring, such as, the permeability of the vessel can change over both space and time within a single vessel and throughout the entire network of vessels [27][28]. Permeability

$$P_{eff} = \frac{J_s}{\Delta C S} \quad (3)$$

can be quantified by using optically labeled tracers, but when using these tracers it is best to think of the calculated permeability as being the effective permeability of that particular tracer and not of the whole system. This can be useful for studying transport of certain tracers, because the uptake into the system could vary depending on the tracer's composition.

2.1.4 Immune Cell Trafficking

The lymphatic system is also extremely important in immune surveillance because the vessels traffic antigen-presenting cells from tissues to lymph nodes [43, 36, 3]. By transporting lymph or fluid to the lymph nodes, the antigen-presenting cells are provided with a wide sample of peripheral antigens [29, 41]. Where these antigen-presenting cells can consist of dendritic cells, macrophages, and B cells [29, 41]. This transport is especially important for maintaining tolerance to self-antigens and for inducing an adaptive immunity [16, 37].

Immune cells and several types of cancer cells secrete the chemokines CCL19 and CCL21 [52]. The cancer cells also have the corresponding receptor CCR7 to the chemokines [52], which, eventually leads to the cancer cells migrating towards the draining lymphatic vessel and are transported to the lymph nodes [10].

2.1.5 Lipid Transport

Almost all dietary lipids enter the lymphatics and are transported to the circulatory system [13]. In the small intestine, non-soluble free fatty acids are reesterified into triglycerides by the enterocytes [13]. These triglycerides are then packaged into soluble chylomicrons that are capable of moving in the bloodstream's water-based solution. The chylomicrons are too large, up to 1200 nm, to be taken up by the surrounding blood capillaries [59] so they are absorbed by lacteals, blind ended lymphatic vessels [59, 13]. Interestingly, lacteals can change their morphology during fasting and non-fasting to adjust to the varying loads [20] and lymph flow changes, due to altering the interstitial matrix tissue hydration, can affect chylomicron transport, where an increase in flow would result in an increase in chylomicron transport [60]. Therefore, it is thought that the lymphatic endothelium might actively regulate dietary lipid uptake [13].

Recently, several reviews have highlighted a potential link between lymphatic function and lipid homeostasis [21, 44, 45, 48, 13]. All dietary lipids enter the circulatory system through the lymphatic system, however, very little is known about the uptake mechanisms involved with this process [13]. While the regulation of material flux through the lymphatic system has been studied extensively, the mechanisms involved and the routes taken have not been as widely explored [3]. This is heavily due to the difficulty involved with seeing and isolating lymphatic vessels in vivo [28]. Therefore, an in vitro model that can recapitulate the biophysical environment seen in vivo could help expand our knowledge.

If these uptake mechanisms were better understood we may be able to take advantage of these transport routes for drug delivery. Orally delivered drugs are very desirable when targeting intestinal lymphatics, because first-pass metabolism can be avoided. This is because substances absorbed by the lymphatics in the gut bypass the liver and go straight into the circulation [42].

2.1.6 Lymphatic Dysfunction and Disease

There are two particular states of dysfunction that are the predominant motivations for the device discussed in this thesis: lymphedema and cancer metastasis. These diseases and how they relate to this project will be further discussed in the following sections.

2.1.6.1 Lymphedema

Lymphedema results from an imbalance in fluid maintenance and transport due to lymphatic failure or blockage which leads to an accumulation of interstitial fluid in a particular limb [40]. This stagnation of fluid leads to hampered immune responses [3] like impaired immune cell scavenging and increases the likelihood of infection [40, 37]. There are two types of lymphedema: primary and secondary. Primary lymphedema is an inherited disease and secondary lymphedema is a result of injury,

surgery, radiation, or infection. In secondary lymphedema, fluid stagnation causes lymphatic hyperplasia to occur [47].

2.1.6.2 Cancer Metastasis

Lymphatics act as a route for dissemination of many types of cancer cells [65, 30, 57, 3, 8, 39]. However, the mechanisms involved with metastasis are not fully understood.[52] While the role of lymphangiogenesis in lymphatic metastasis remains unclear [9, 53, 64, 66], it is suggested that aggressive tumors secrete lymphangiogenic growth factors in order to induce lymphangiogenesis [23, 34, 54]. The increase of growth factors would enhance lymphatic metastasis and aid the dissemination of cancer cells.

2.2 Current Tissue-Engineered Models

Two transwell systems inspired the design of the device discussed in this thesis. The first is centered around studying lipid uptake mechanisms while the second looks at cancer cell migration.

2.2.1 Transwell Systems

A transwell, as depicted in figures 1, 2, and 3, is a porous membrane attached to an insert placed inside a chamber. The membrane acts as a substance for cells to adhere to and provides a permeable barrier that is useful for distinguishing the effects to the apical and basal transport across the cells. One of the biggest advantages to transwells are the ability to isolate the response from a single cell type while still producing concentration gradients basally or apically. This is not possible with in vivo systems [47, 13]. Such 3D tissue-engineered models are capable of recapitulating crucial aspects of in vivo models while providing the ability to use human cells. The use of transwell systems has led to major contributions in lymphatic research as well as several different systems [18, 24, 25, 52, 13].

2.2.2 Transwell System for Studying Lipid Transport

As mentioned in the Lipid Transport section, lipid uptake mechanisms are not fully understood. So a tissue-engineered model of the lacteal, intestinal initial lymphatics, has been developed to study the uptake mechanisms of lipids into the lymphatic system. This model uses lymphatic endothelial cells (LEC) and an enterocyte cell layer, differentiated Caco-2 (human colon carcinoma) cells, to mimic the enterocyte and lacteal interface [13]. Figure 1 shows a basic schematic of the two cell layers separated by a porous membrane in a transwell system.

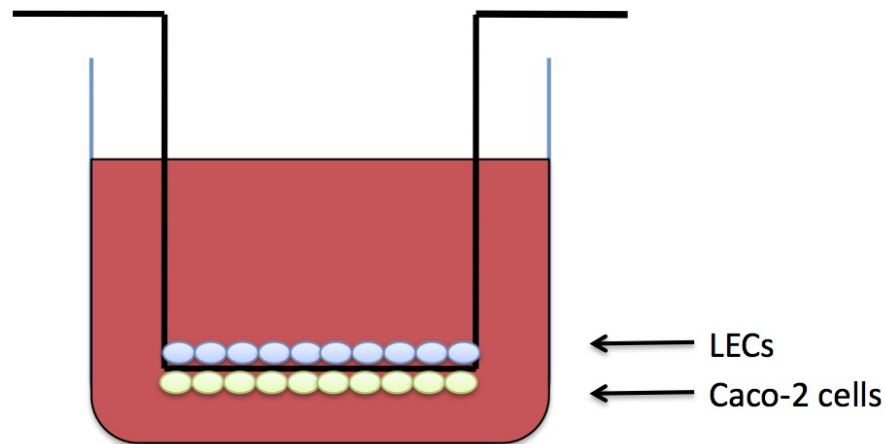


Figure 1: Schematic of Cell Layers in Transwell System

This model has been used to study lymphatic function in lipid trafficking [13]. It is especially useful for determining the overall affects of varying lipid content, lymphatic permeability, and transport routes [13]. Fluorescently labeled dextran and bodipy were used to quantify permeability across the membrane of the transwell with LECs, Caco-2's, and both cell types present. Dextran is a standard diffusive imagable molecule used to characterize concentration gradients and bodipy is a 16 carbon chain fatty acid used to quantify lipid uptake. In this transwell system, the effective permeability was measured to be around $P_{eff}=0.005 \mu\text{m/s}$ for bodipy and $P_{eff}=0.065 \mu\text{m/s}$ for 3 kDa dextran [13].

The model also has the benefit of being able to separate the two cell layers to test the response of one cell type to different stimuli. For instance, the secretions from a transwell with only Caco-2 cells were collected and then introduced to a transwell with only LECs. This can be helpful in potentially decoupling responses from different cell types to establish the individual roles of each. This tissue-engineered model establishes a strong foundation for studying the uptake mechanisms of lymphatic vessels.

2.2.3 Cancer Metastasis

Lymphatics play a significant role in cancer cell dissemination [52]. Unfortunately, the mechanisms involved with this process are not fully understood. So a transwell based model was used with cancer cells to show migration to lymphatics. In this model a collagen gel with cancer cells suspended in it was used to create a three-dimensional interface with LECs on the other side of the porous membrane [52]. Where the collagen gel acts like the interstitial space that the cancer cells migrate through to get to the draining lymphatic vessels. Refer to figure 2 for a detailed schematic.

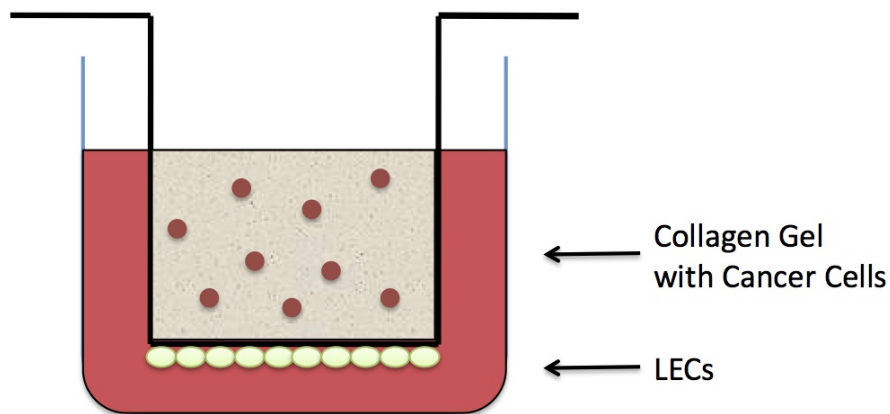


Figure 2: Schematic of LEC Layer and Cancer Gel in Transwell System

Shields et al. found an increase in cancer cell migration when transmural flow, 0.1 to 0.8 $\mu\text{m/s}$, was present, see figure 3 [52], which was in the range of interstitial flow

in vivo. The cancer cells secrete CCL19 and CCL21 and also have the receptor CCR7 present for these ligands. When flow is present a concentration gradient of CCL19/21 forms around the cells, see figure 4, which serves to direct their migration [52]. This response is heightened in the presence of other cells that also have CCR7 signaling [52]. CCR7 is also present in lymph node metastasis with breast cancer[6], melanoma [56, 63], colorectal [19], esophageal squamous cell [11], prostate [26], head and neck [62], non-small lung [55], and gastric cancers [35, 52]. This model helped show the importance of flow and its potential role in tumor cell homing to lymphatics, because interstitial flow is always directed towards the nearest draining lymphatic.

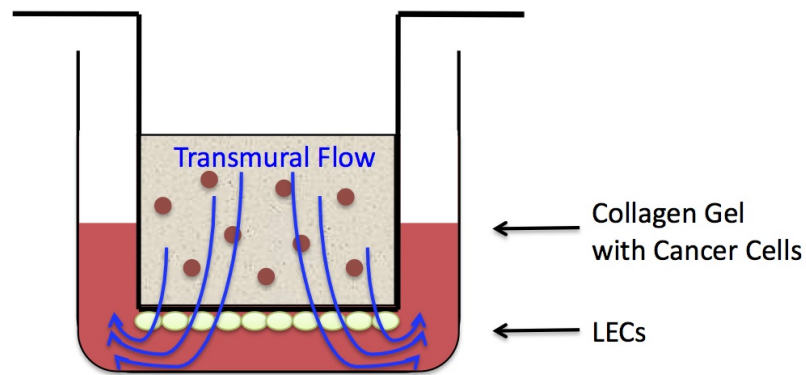


Figure 3: Schematic of LEC Layer and Cancer Gel in Transwell System with Transmural Flow

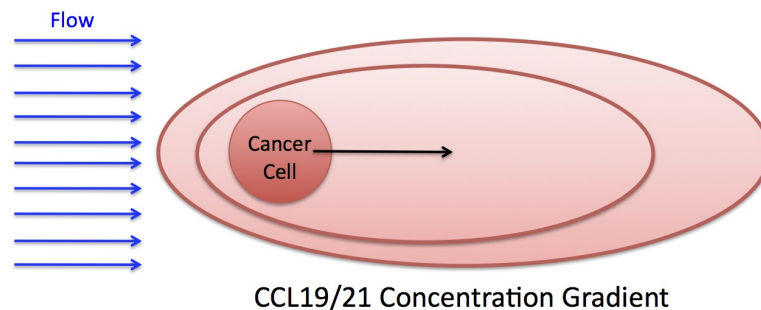


Figure 4: Concentration Gradient of CCL19/21 Due to Presence of Flow

2.3 Importance of Flow

Interstitial flow, 0.1 to 1 $\mu\text{m/s}$ [37], has been shown to have profound effects on lymphatic function [13, 28, 37, 46, 17]. We know that both diffusion and convection play a role in solute movement[28]. It is also important to recognize that lymphatic exchange is dynamic and is subject to acute regulation as well as chronic adaptation depending on the stimulus [28], such as inflammation or fasting/feeding states. To further state the dynamic nature of lymphatics, the actions taken by the lymphatic capillaries following an injury or during inflammation is determined by the type of immune response triggered [29]. Furthermore, vasoactive agents can induce gradients in the tissue space by altering permeability and contractility properties [28].

With rapidly growing tumor cells or during inflammation the vascular permeability severely increases and this results in an increase in lymph flow [37]. Another indicator of the importance of flow is how sensitive transport is to changes in pressure [13]. From Starling's Law, equation 1, we know that the direction and magnitude of lymph flow is dependent on the pressure gradient [32, 50, 58, 3]. From these statements we can see that changes in pressure and permeability affect lymphatic transport in both magnitude and direction. Changes in either of these properties or both could result in better fluid reabsorption across the lymphatic endothelium [28].

During inflammation, permeability, interstitial fluid pressure, and lymph flow all increase [4, 22, 5, 38]. It is likely that the increase in flow, and therefore fluid and cell transport, acts as an early mediator and signal for inflammation [37].

Transmural flow, see figure 3, was used to observe cancer cell migration [52]. During this study, Shields et al. found that in static conditions LECs induced CCR7 chemotaxis of tumor cells, but in transmural flow without LECs they had an increase in tumor cell migration and it was still CCR7 dependent [52]. Of the four cell types they tested, ZR75-1 and MDA cells reacted the strongest to the transmural flow [52]. Low levels of transmural flow have also been shown to increase lymphatic permeability,

dextran transport, aquaporin-2 expression, and dendritic cell transmigration [37].

At this time, the effects of flow have not been researched as extensively as they should be [37]. Basic functions cannot be performed without flow present. For example, in order for lymphangiogenesis to occur in adult mice, interstitial flow must be present [46] and in disease states, when interstitial flow is weaker, VEGF is unable to aid cells as effectively as in a normal state [17]. During times such as inflammation or fasting and feeding states the lymph flow can drastically change which results in changes to lymphatic function. Permeability and contractility are directly affected by flow and so is the transport of fluids and cells as well as immune cell trafficking [37]. Therefore, flow is definitely an important factor in lymphatic function and should be further explored.

2.4 Variations of Current Tissue-Engineered Models

The following two sections propose ways to incorporate both luminal and transmural flow into current systems. This allows for a more biophysically accurate environment as well as continually monitoring optically labeled tracers or cells throughout an experiment.

2.4.1 Lipid Transport

Figure 5 shows the first model. This model is a modification of the previously mentioned lipid uptake transwell system that includes luminal and transmural flow. The previous model was used to study lipid uptake mechanisms, but could not be used to study changes in permeability in the presence of luminal flow. However, this model could be used for permeability studies as well as characterizing the affects of shear with lipid uptake. This device can also be used for drug screening, lipid uptake, and lymphedema studies. Lymphedema is known to have leaky vasculature which results in fluid leaving the collecting lymphatic vessels. The progression of how the leaking vasculature affects permeability will be the predominate focus of this device at this

time. Physically relevant shear stresses will be used for this disease model. Dixon et al. found that shear stress is 0.64 ± 0.14 dyne/cm² in lymphatics [12].

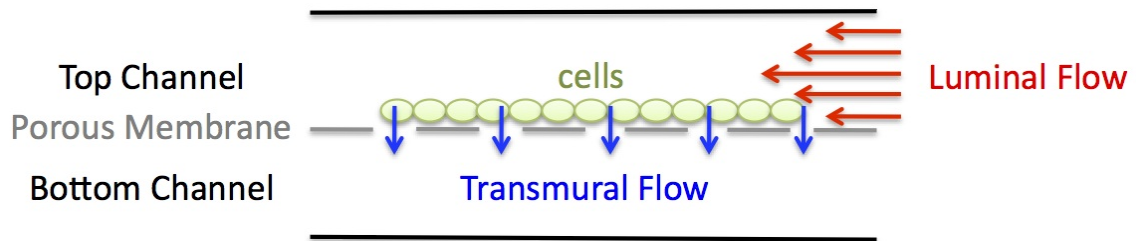


Figure 5: Flow through porous membrane with luminal flow and transmural flow present

2.4.2 Cancer Metastasis

A slight modification to this flow system could allow for better cancer cell migration quantification. Shields et al. was able to do an end time quantification of cancer cell migration, but this method only results in the number of cancer cells that made their way to the membrane in the transwell and stayed on the membrane. It does not specifically count the cells that migrated through the membrane, cells that were on their way to the membrane, motility of the cells, or overall directionality of the cells. A live cell system that could image and quantify cell migration throughout the experiment could account for these additional variables. Figure 6 is a modification of the previous model to allow for a fluid column that could induce a hydrostatic pressure gradient that would correspond to transmural flow through the collagen gel with cancer cells suspended in it.

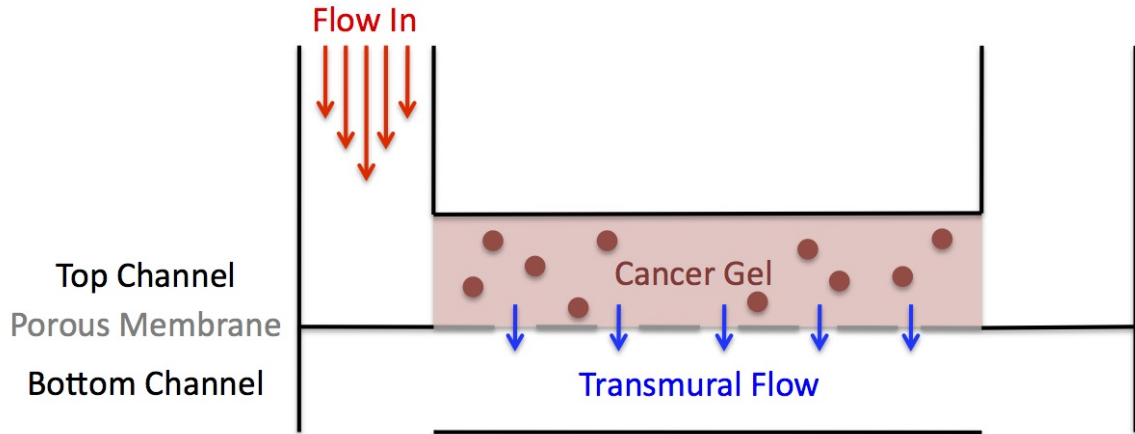


Figure 6: Flow through collagen gel with cancer cells suspended in the gel

2.5 *Project Requirements*

From this literature review there are several obvious gaps in our current understanding of flow and its role with lymphatic transport. Several groups have reported the significance of flow and its affect on permeability and yet so little has been done to incorporate flow into in vitro models. If we understood how flow influences permeability we may have a better idea of how lymphatics respond to flow in cases of dysfunction, like lymphedema. Another heavily emphasized lymphatic characteristic is its dynamic nature and yet no models are currently capable of imaging these dynamic properties in real time.

So for this project, flow channels that support the 3D architecture seen in transwells, induce relevant lymphatic shear stresses, and induces relevant interstitial flow rates will be designed and tested. This requires the use of porous membranes, flow channels, and the capability to image real time. The following three specific aims were established for this device.

Aim 1: Device creates physiological relevant environment under which cells can be cultured and are viable.

Aim 2: Device allows for quantification of effective permeability.

Aim 3: Device can be used to quantify cell migration.

The first aim establishes that cell culture can actually be done in this device and that the cells are viable during experiments. The next aim is to ensure that permeability can be quantified in the channels. This is really important for establishing a foundation for all future studies involving variations of lipid uptake. The final aim creates a novel quantification system for measuring cell migration in real time. This is important for measuring overall motility and flux of migration.

2.5.1 Similar Devices

Recently there have been a couple of flow chambers similar to the device featured in this thesis. Almost all of them use a porous membrane and support the capability to induce flow, but each have their limitations and do not satisfy the needs of this project.

The first device is a lung on a chip, see figure 7. This device has a simple design, with the membrane made from polydimethylsiloxane (PDMS) [14]. While convenient, PDMS molds have limitations on how small the features can be so extremely small pore sizes are very challenging with this technique. For this project we would like to be able to implement commercially available membranes allowing us to use a wide variety of pore sizes and making its implementation highly flexible. Another limitation with this device is the overlapping channels. As it is very challenging distinguish changes in fluorescent concentration for individual channels when they are overlapping.

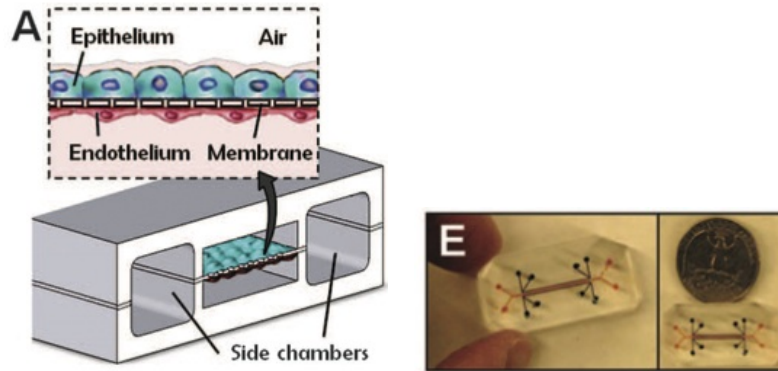


Figure 7: Lung on a chip cross sectional view and top view[1]

The next device is significantly more complex than necessary for this project, see figure 8. In this device, there is a cell culture side and a flow side that are separated by a membrane [51]. Flow cannot be actively controlled on the cell side so luminal flow is not a possibility with this device and cells can only be cultured on the cell side. This does not allow for a co-culture on both sides of the membrane. One really interesting aspect to the design is the gradient generator which allows for on-chip control of the flow through the flow channel [51]. Unfortunately, very large flow rates cannot be achieved.

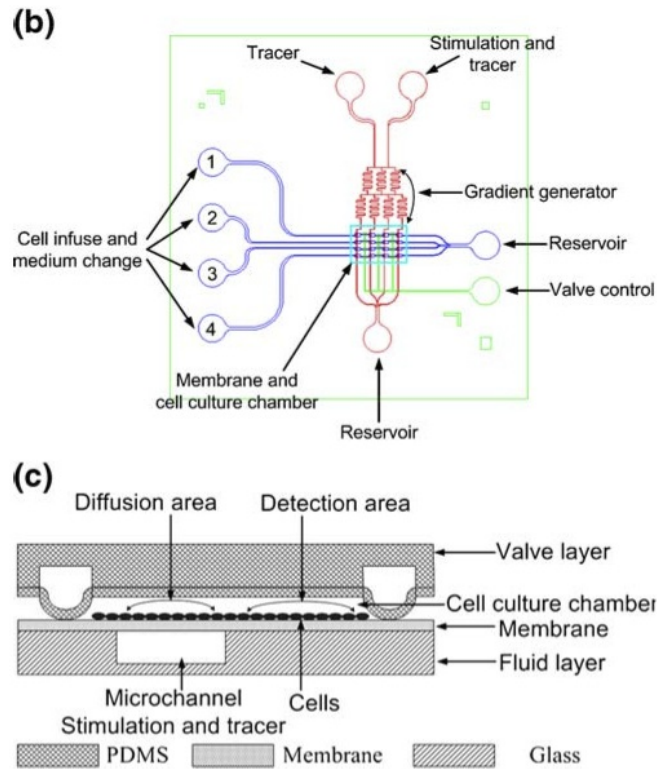


Figure 8: Schematic of flow channels with view of membrane layers[2]

There are a few other devices like these that incorporate membranes and flow, but most either use the pneumatic air valves to control small amounts of flow or rotor bars to recirculate fluid. To my knowledge, there isn't a device that supports cell culture on both sides of a permeable membrane as well as controlling both transmural and luminal flow.

CHAPTER III

METHODS

3.1 Design and Fabrication

Throughout the design of this device, there have been several points of consideration. First, there were a number of specific design requirements for useful and effective experimentation. Next, I had to incorporate these necessary factors into a design that could be easily manufactured and also functional for imaging. This chapter will focus primarily on the evolution of the device as each one of these areas are explored and then the methods involved with cell culture and imaging. In this section, the design requirements will be stated and explained. Followed by adjustments for ease of manufacturing and then final changes for enhancing imaging.

3.1.1 Design Requirements

As mentioned in the previous chapter, the primary requirement was to be able to induce both luminal and transmural flow over two separate cell regions that share a common interface through a porous membrane. We need to be able to induce interstitial flow, 0.1 to 1 $\mu\text{m/s}$, through the membrane, induce physically accurate shear stress values, $0.64 \pm 0.14 \text{ dyne/cm}^2$ for luminal flow, culture multiple cell types on either side of a porous membrane, have the option of incorporating cells into a 3D construct such as a collagen gel, and these cells need to be able to signal across this membrane. We also want the flexibility of pore sizes available with commercially available polycarbonate membranes. For the two outlined models a 3 μm pore size will be used for the permeability model and a 8 μm pore size will be used for the cancer migration model. The larger pore sized membrane will be used for the cancer migration model so cancer cells can migrate through the membrane.

Aside from reducing sample size, microfluidic devices also need to be scalable for high-throughput experimentation. The minimum number of test sections for the device was set at four channels with the intent to scale up later. This allows for two channels to be static, control channels and the remaining two channels to have flow. Finally, we wanted the inlets and outlets to be separable so drug screening could be performed in the future.

3.1.1.1 Prototype 1

In my first design, I wanted all of the outlet channels to be in the same field of view for imaging. This constraint required the fluid in each channel to be at the same time step as the other channels, because all of the channels would be imaged together and discrepancies due to time would cause unnecessary complications. The bottom channel consists of 1 mm diameter straight channels that eventually converge in to smaller channels. See figure 9 for COMSOL (COMSOL, Inc., Burlington, Massachusetts) models of the bottom and top channels. The top channel behaves in a similar manner, however, it begins with a dip that crosses over the bottom channel. This lower section, 1 mm² area, is where any cell interactions would occur.

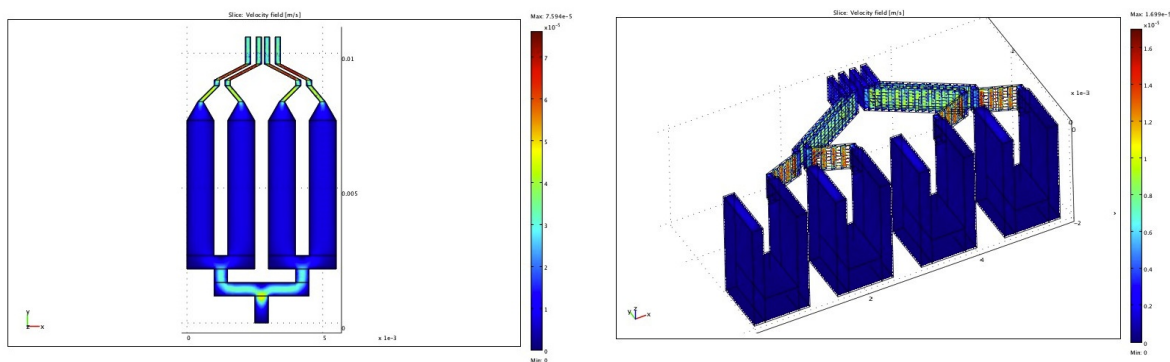


Figure 9: Comsol rendering of flow in the bottom (left) and isometric (right) channels of prototype 1

Table 1 shows how well this prototype fulfills the design requirements as defined earlier.

Table 1: Fulfillment of Design Requirements by Prototype 1

Feature	Satisfied
Physiological Transmural ($0.1 \mu\text{m/s}$) and Luminal ($\tau=0.5 \text{ dyne/cm}^2$) Lymphatic Flow	✓
Co-Culture Cells	✓
3 or 8 μm Porous Membrane	✓
Four Channels	✓
Separate Inlets and Outlets	

3.1.2 Manufacturing Requirements

I decided the best approach for creating these devices would be PDMS cast in reusable molds. I decided to mill out these molds from aluminum, because milling is significantly easier to do than lithography and this also allows for much larger feature sizes. I chose aluminum because it is easy to cut and it can withstand the heat from the PDMS curing process (60°C).

When machining a part, the end mill diameter and your fillet allowances play a huge role in machining time and quality. A short distance between channels requires a shorter diameter end mill and smaller diameter end mills are more expensive, less durable, and have a shorter cutting length. They also take a lot more time to cut out a small section of material than a larger end mill. Limiting the number of tools used during the mill job is also desirable, because each tool has to be zeroed to the surface of the part and if these tools are not precisely zeroed then discrepancies will exist in the depths cut in the part. Depending on how small the tools are, these discrepancies could prove to be disastrous. There could also be inconsistencies in the surface finish. This is especially important in microfluidic devices, because you want as smooth

a surface as possible for binding PDMS layers together. The other characteristic associated with end mills is the fillet size. Depending on the design, a large fillet could ruin whatever geometry was in the design. To avoid drastic changes, smaller end mills can be used, but the same problems previously stated will arise. What I ultimately determined was less complex designs are much easier to manufacture.

Making the mold is the hardest part of manufacturing for this device, but it is not the only aspect to fabrication. Once the molds are made they have to be attached to one another and the porous membrane needs to be placed in between the channels. A plasma cleaner is used to attach PDMS to PDMS. During the plasma treatment, the PDMS is temporarily made hydrophilic so it can bond to itself. The plasma treatment is useful, because it only affects the near surface, there is no organic residue, and it can work on rough, porous, or uneven surfaces. Once the PDMS is plasma treated the exposed surfaces must be aligned and connected. Depending on the design, this could prove to be quite difficult. Unfortunately, the commercial membranes from Millipore (Millipore, Billerica, Massachusetts) do not attach to PDMS when plasma treated. Which means placing them between two layers of plasma treated PDMS, chemically attaching them, or suspending them in the PDMS mold while it is curing are the best options for incorporation. The first three prototypes discussed in this thesis are significantly smaller than the half inch membranes, which means if the membranes were simply placed between two layers of cured PDMS the ridges of the channels would not adhere to anything and the device would most likely not retain its shape and fluid would leak between the layers. Chemically attaching the membrane could also be problematic due to biocompatibility constraints, but has been done by other groups. Finally, having the membrane suspended in PDMS while it is curing presents its own problems. For instance, PDMS could soak the membrane and clog the pores. This is avoidable if the interface region is tightly clamped on the membrane.

3.1.2.1 *Prototype 1 Revisited*

Once I had an initial design, I went on to design the molds to be used for casting, see figure 10. Due to the complex geometry of the top channel, a bridge that locks into the top mold had to be designed in order to complete the mold, see figure 11.

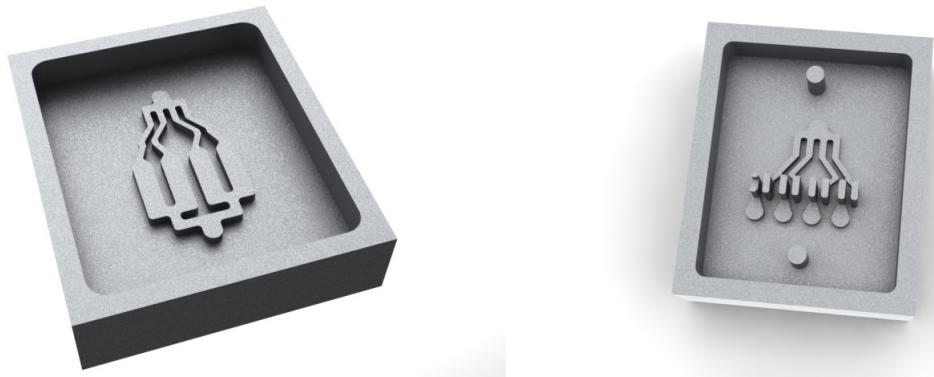


Figure 10: Molds for bottom (left) and top (right) channels



Figure 11: Bridge for top mold

One major disadvantage to this design is the distance between the outlet channels. The largest end mill I could use to cut between these channels was 0.009 inches in diameter. With such a small cutter, I would only be able to cut down 0.0045 inches which would not be deep enough for my channels. Another disadvantage was interfacing with the tubing. The tubing diameter was 0.95 mm and no tubing connectors could be found to scale up the tubing size. Seeding cells would be difficult with this device as well. Finally, incorporating the membrane would require treatment to ensure adherence, something we wanted to avoid if possible.

Ultimately, this device was not ideal for manufacturing.

3.1.2.2 *Prototype 2*

The previous prototype was too difficult to mill out so this prototype was designed with simpler geometric features. This prototype has separate inlets and outlets along with collagen access channels to help with seeding cells. These access ports allow placement of collagen treatment directly over the interface which allows for direct placement of cell seeding. Figure 12 shows a 3D rendering of this prototype and a top view.

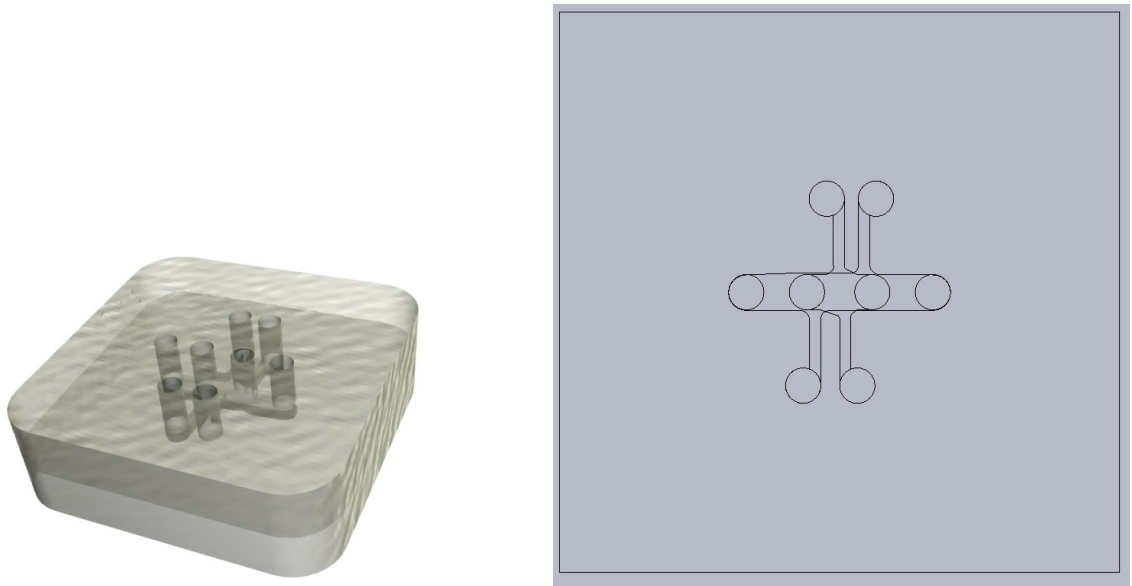


Figure 12: 3D rendering of actual device (left) and top view (right)

Some problems still exist in this design, like how to incorporate the membrane, very small end mills have to be used (1/32 inch), and four tools needed to be used, but overall this prototype was a huge improvement over the last and was feasible for manufacturing. Figure 13 shows the bottom and top molds. The bottom mold had to be an inverse of the actual design so that when the two layers were plasma treated together the overlay would be correct. PDMS was cured in these molds and could

be attached together with plasma treatment. While this device was an improvement, there were still several problems that needed addressing, such as membrane incorporation and scaling up the number of test sections, see table 2.

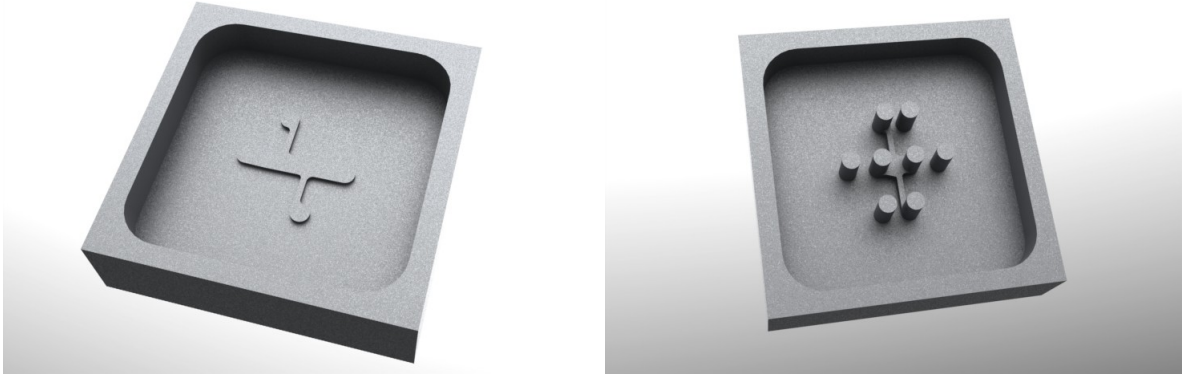


Figure 13: Molds for bottom (left) and top (right) channels

Table 2: Fulfillment of Design Requirements by Prototype 2

Feature	Satisfied
Physiological Transmural ($0.1 \mu\text{m/s}$) and Luminal ($\tau=0.5 \text{ dyne/cm}^2$) Lymphatic Flow	✓
Co-Culture Cells	✓
3 or $8 \mu\text{m}$ Porous Membrane	✓
Four Channels	
Separate Inlets and Outlets	✓

3.1.2.3 Prototype 3

Prototype 3 was further simplified from prototype 2 and the top and bottom channels became mirror images of one another. This new X shape allows for flow channels and collagen access channels, see figure 14. The biggest improvement was how the membrane was incorporated. Instead of including the tubing connecting columns in the mold, both the top and bottom channels were placed on either side of the membrane

and PDMS was filled in around the membrane. This allows for the membrane to be suspended between both channels in the same layer of PDMS and actually curing the membrane in the PDMS. See figure 15 for the molds.

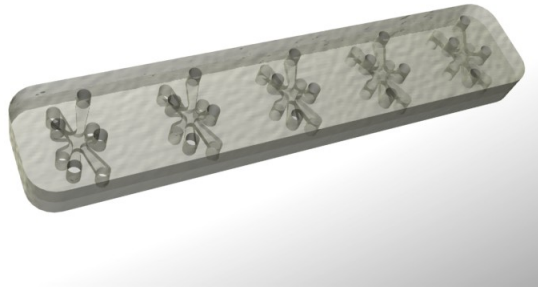


Figure 14: Rendering of actual device

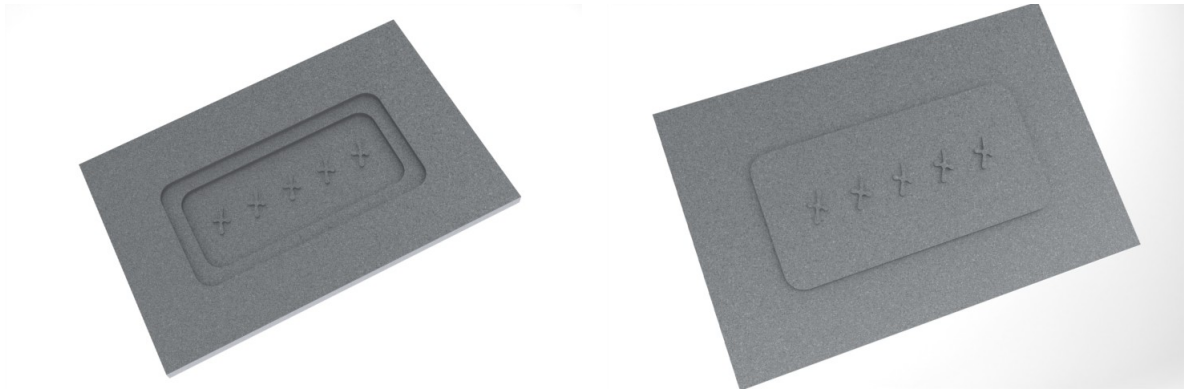


Figure 15: Molds for bottom (left) and top (right) channels

Unfortunately, inserting the top mold into the bottom mold did not provide enough pressure on the membrane and PDMS would leak and coat the membrane clogging the pores. To fix this problem, a slight modification was made to the molds. Both the top and bottom molds were modified to be flush against each other and screws tightened the two pieces together to provide enough force to keep the PDMS from leaking into the membrane. An access hole was included in the top mold so

PDMS could be filled into the mold. See figure 16. An additional cap mold was made for the tubing interface holes.

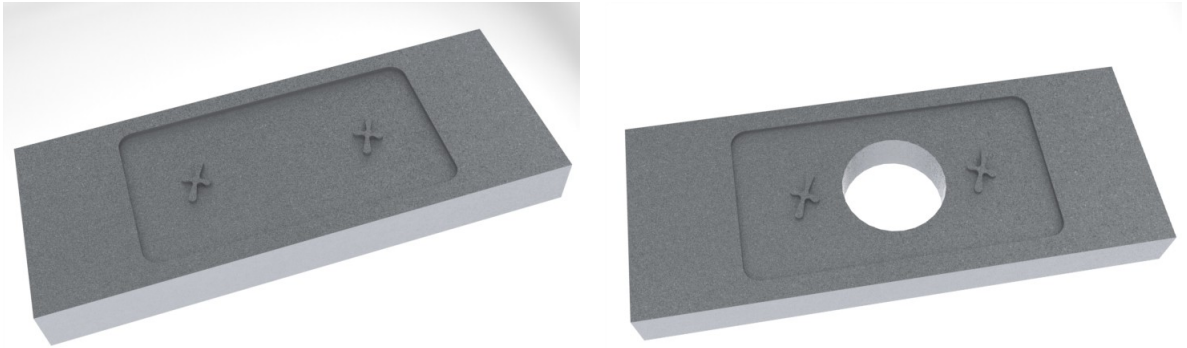


Figure 16: Molds for bottom (left) and top (right) channels

This modification kept the membrane from being covered with PDMS and was successfully integrated into the device. However, the access hole created a new problem. The meniscus formed from the hole created an extremely flimsy layer that was prone to tearing and if too much PDMS was put in the device a large bubble would form, see figure 17. Either way the tubing cap could not be easily applied to the device which meant interfacing with the device was still problematic. This device did satisfy all of the design requirement, see table 3, however interfacing was not trivial so a final design was made.

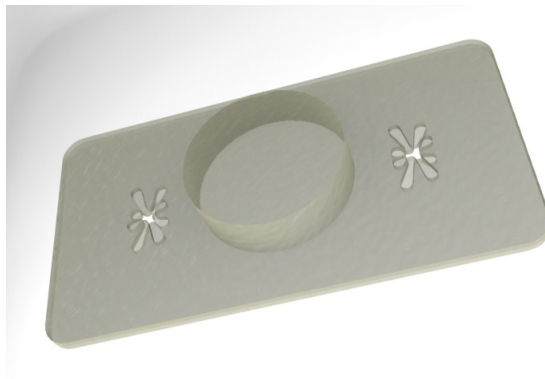


Figure 17: Rendering of modified prototype 3

Table 3: Fulfillment of Design Requirements by Prototype 3

Feature	Satisfied
Physiological Transmural ($0.1 \mu\text{m/s}$) and Luminal ($\tau=0.5 \text{ dyne/cm}^2$) Lymphatic Flow	✓
Co-Culture Cells	✓
3 or 8 μm Porous Membrane	✓
Four Channels	✓
Separate Inlets and Outlets	✓

3.1.2.4 Prototype 4

Prototype 4 involved a completely new approach. Once I had a working prototype that could incorporate the membrane, I wanted to focus on interfacing with the device. I decided to create a stand that would act as a device housing and could exert a clamping force on the device. With this stand I could integrate PDMS tube holders that would be aligned by the stand over the channels. Then to provide mechanical support while maintaining optical clarity, I would clamp a slide over the channels. See figure 18 for an exploded view of the stand and device and for a clamped view.

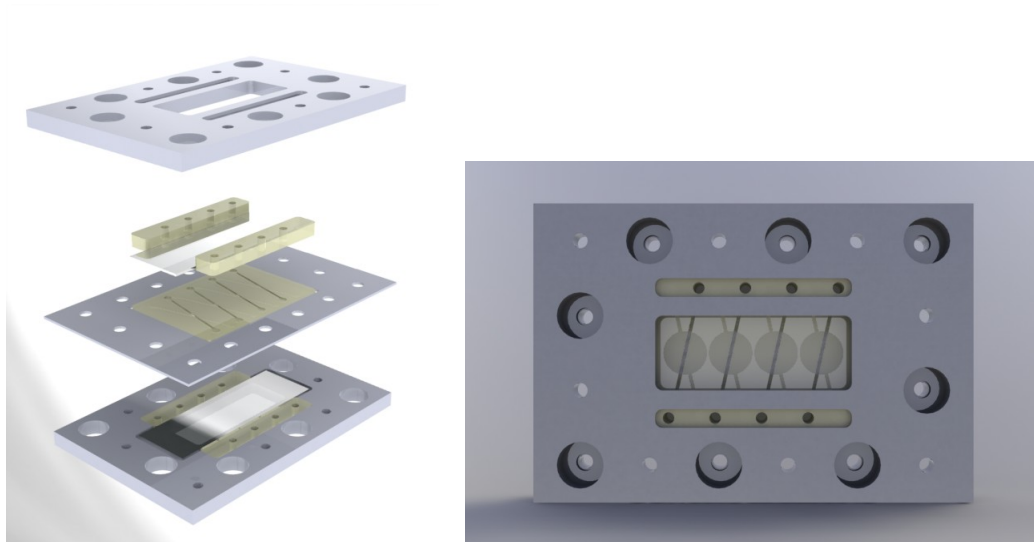


Figure 18: Exploded view of the device (left) and clamped together view (right)

The stand uses two different components, a cap and the middle piece. Both the top and bottom caps are identical, but when placed face to face they can lock together, see figure 19 left side, with the use of the middle piece. Another interesting characteristic to the cap is that both the tubing holders and slide fit into milled holes. This can be seen clearly in figure 18. The second stand component is the middle piece, figure 19 right side. This piece acts as the connector and clamp. It is slightly thinner than the membrane PDMS piece and it provides the surface that locks the caps in place. This locking mechanism allows for the top and bottom caps to be independent from one another. This allows for independent seeding of cells on either side.

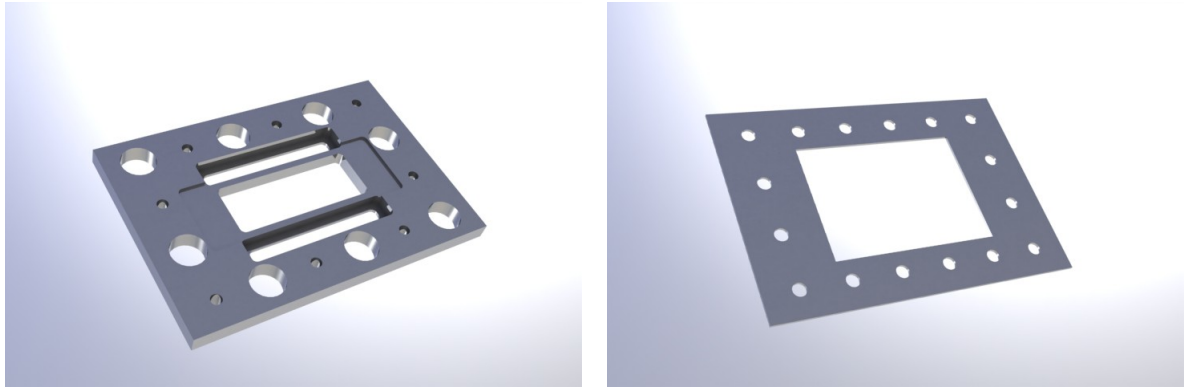


Figure 19: Cap (left) and middle (right) of stand

For the device, the mold of the channels was made in a similar way as the previous prototype. Two, flush, mirror image channels are screwed together with a membrane place between the channels, see figure 20. However, instead of filling the PDMS from the top or bottom a gap was milled on the side of the mold so PDMS could be injected from the side. Any discrepancies due to overfilling can be cut off. Figure 21 shows a rendering of the membrane layer as well as a cross-sectional view of the flow regimes and cell placement.

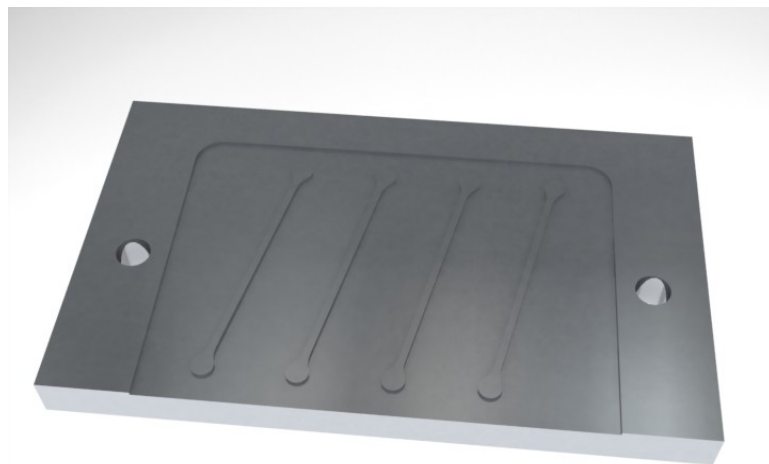


Figure 20: Mold for channels in prototype 4

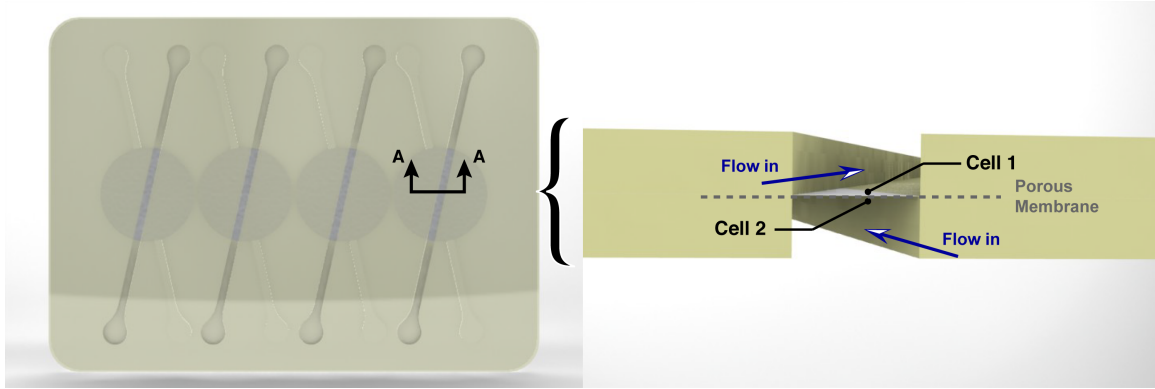


Figure 21: Cross-sectional view of flow in prototype 4

The individual components in this prototype worked great, however, the interface between the tube holders and slide was subjected to perpetual leaking. To resolve this issue, the tube holders were modified to act as a cap to the channels, figure 22 left. Figure 22 right shows the mold for this component. This solution fixed the leaking problem, but if too much flow was added the PDMS layers occasionally separated. This generally happened around 1 mL/min flow rate which corresponds to $\tau_w=2.86$ dyne/cm², see equation 4. Table 4 shows how well prototype 4 fulfilled the device requirements.

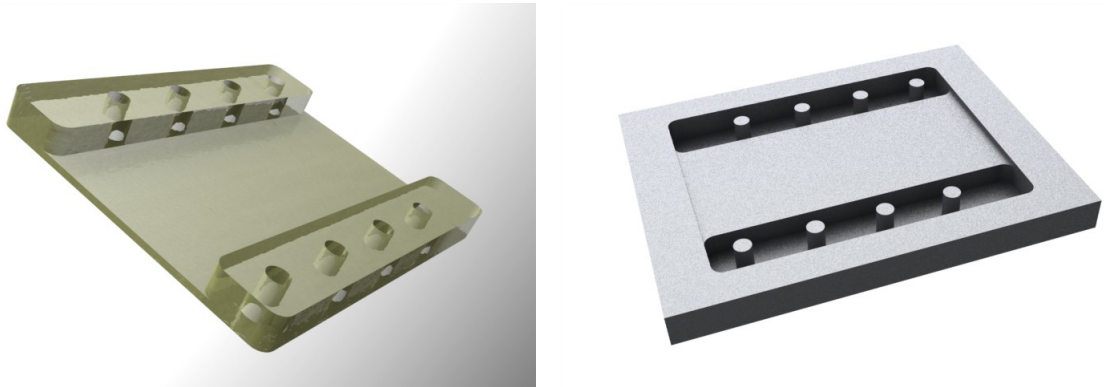


Figure 22: PDMS channel cap (left) and mold (right)

For rectangular ducts, equation 4 is used to calculate shear stress τ (Pa) from the flow rate Q (m³/s), dynamic viscosity μ (Pa·s), width w (m), and height of the

channel h (m).[61]

$$\tau = \frac{6Q\mu}{wh^2} \quad (4)$$

Table 4: Fulfillment of Design Requirements by Prototype 4

Feature	Satisfied
Physiological Transmural (0.1 $\mu\text{m/s}$) and Luminal ($\tau=0.5$ dyne/cm ²) Lymphatic Flow	✓
Co-Culture Cells	✓
3 or 8 μm Porous Membrane	✓
Four Channels	✓
Separate Inlets and Outlets	✓

3.1.3 Imaging

Once I had a working device that I could seed cells on and induce flow without leaking, I needed to be able to image the device.

3.1.3.1 Prototype 4 Modified

I had to modify prototype 4 to enhance its imaging capabilities. The metal caps were in the way of the lens and the PDMS layers had the potential to separate. So I modified the stand. Instead of using aluminum, I used acrylic and kept the acrylic over the viewing area of the device. This acrylic cap layer provides a clamping force on the PDMS layers to keep them from separating. As an added measure, the PDMS layers were plasma treated together. This meant that collagen could not be applied only over the intersection and cells could not be limited to the intersection. To keep the acrylic surface as clear as possible, the holes for the tube holders and screw holes were the only areas milled. Therefore, the middle section had to increase in thickness to account for the PDMS channel cap that was previously embedded in the stand

cap, see figure 23. Table 5 shows that this final modification satisfies all requirements for the device as well as the imaging constraints. Finally, figure 24 shows the actual device and stand with food coloring in the channels.

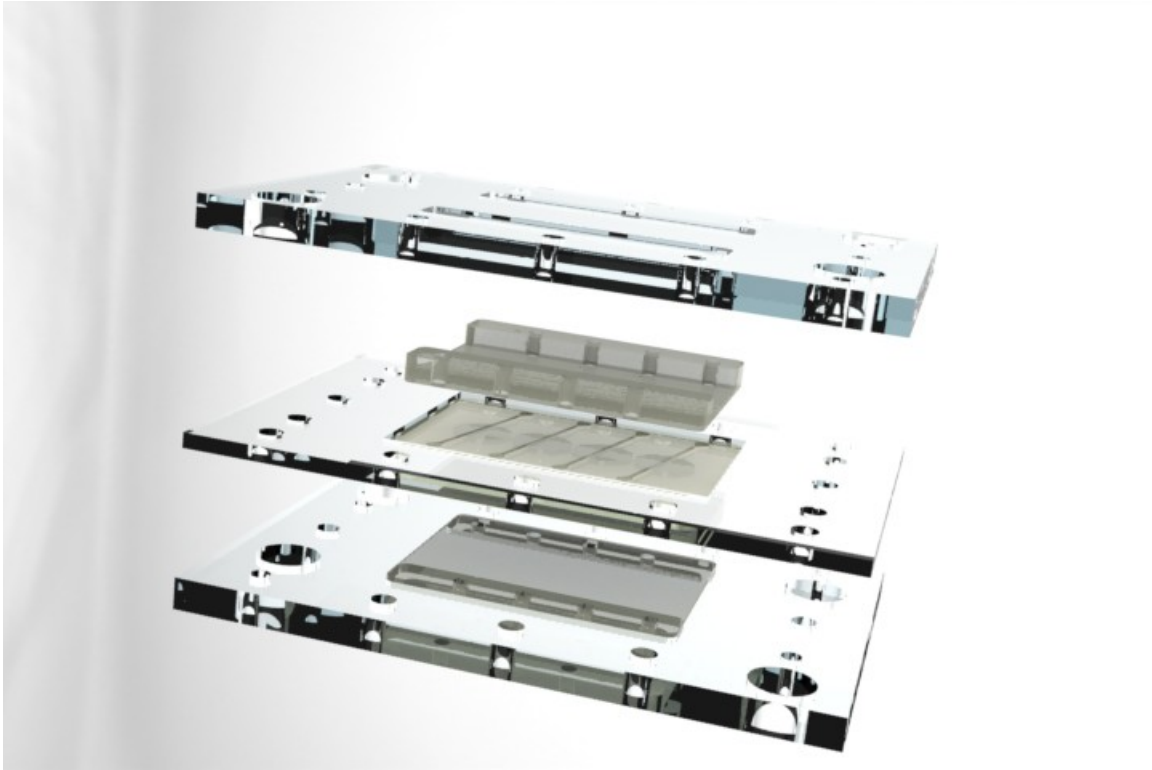


Figure 23: Exploded view of final device and stand

Table 5: Fulfillment of Design Requirements by Modified Prototype 4

Feature	Satisfied
Physiological Transmural ($0.1 \mu\text{m/s}$) and Luminal ($\tau=0.5 \text{ dyne/cm}^2$) Lymphatic Flow	✓
Co-Culture Cells	✓
3 or $8 \mu\text{m}$ Porous Membrane	✓
Four Channels	✓
Separate Inlets and Outlets	✓

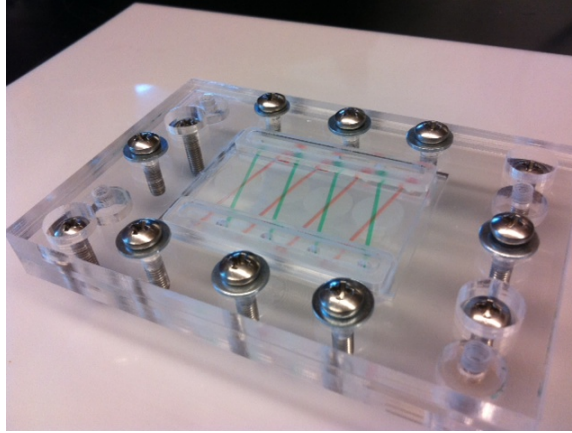


Figure 24: Actual device with dyed channels

After several tests with this device, I found that I would get unwanted aberrations during imaging. The two outside channels achieved better clamping while the two inside channels appeared fuzzy, see figure 6. Another disadvantage was that the attached PDMS cover distorts viewing of cells, because of mill lines and dust accumulation. To fix this problem, I went back to using a slide over the viewing area. To prevent leaks I added a lip to the tube holder that I could plasma treat to the slide, see figure 25 (left). Figure 25 (right) shows the mold for this modification. After plasma treating the tube holders to the slide, I applied a thin bead of PDMS to the intersecting line and I let it cure for an hour at 60°C. Next, I plasma treated the glass top and bottom pieces to the membrane piece. Finally, to apply flow I inserted it into a clamp, see figure 26. The clamp allows for flows as high as 17 mL/min before the device fails, which corresponds to a 48.57 dyne/cm². This final modification not only satisfied all of the goals, but also made the images look cleaner and more crisp, see figure 6. See table 7 for the complete checklist.



Figure 25: Assembly of membrane with slides and tubing connectors (left) with tube holder mold (right)

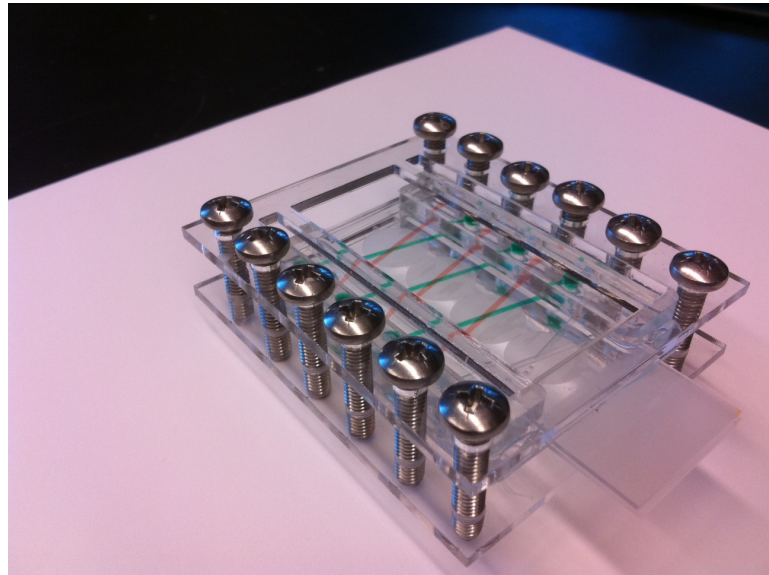


Figure 26: Final prototype with clamp and dyed channels

Table 6: Images from final modification of prototype 4. 4 different dextran channels

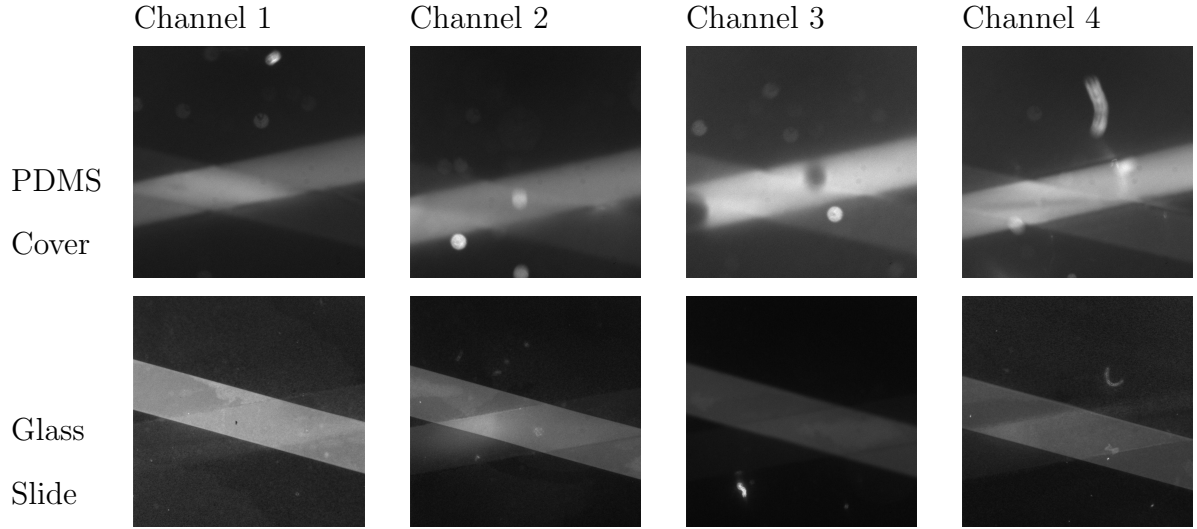


Table 7: Fulfillment of Design Requirements by Final Prototype 4

Feature	Satisfied
Physiological Transmural ($0.1 \mu\text{m/s}$) and Luminal ($\tau=0.5 \text{ dyne/cm}^2$) Lymphatic Flow	✓
Co-Culture Cells	✓
3 or 8 μm Porous Membrane	✓
Four Channels	✓
Separate Inlets and Outlets	✓

The final device can support transmural and luminal flow through its channels and it can withstand significantly higher flow rates than those associated with lymphatics. Cell culture can be done in this device and its identical channels ensure the ability to culture cells on either side and allows for co-culture across the membrane. Commercially available polycarbonate membranes can be incorporated into this device. This device has four channels and the capability to easily scale up the number of available

channels. Finally it has separate inlets and outlets, which allow for separate testing conditions across the channels, a feature particularly useful for drug screening. The final design satisfies all of the design requirements and is easy to manufacture.

3.2 Device Preparation

3.2.1 PDMS

A Dow Corning Sylgard 184 Elastomer Kit (Dow Corning, Midland MI) was used for PDMS. This kit consists of two parts: base and curing agent. A 10:1 ratio of base to curing agent was used. This solution would then be mixed with a vortex mixer. Once mixed the PDMS solution would be poured into the molds and then the molds would be placed in a vacuum chamber for at least 20 minutes so all of the bubbles could be removed. After all the bubbles were removed the mold would be placed in the oven at 60°C for at least 4 hours.

3.2.2 Plasma Treatment

Once all of the components were cured they were removed from their molds, the attachment side were taped with clear tape until all of the dust was removed. Then the PDMS and glass slides were placed on the glass slab in the plasma treater, attachment side up. Air was evacuated from the plasma treater for 2 minutes and then the plasma treater was be turned to high and a release valve was opened until a magenta color appeared in the chamber, after which the components were plasma treated for an additional two minutes. Afterwards, everything is turned off and air is slowly let back into the chamber. Then the prepared pieces were aligned and stuck together.

3.3 Cell Culture

3.3.1 Lymphatic Endothelial Cells

An Endothelial Cell Basal Media (EBM) solution is used as media for the LECs and is supplemented with 20% FBS, 1% Glutamax, 1% penicillin-streptomycin, 25

$\mu\text{g}/\text{mL}$ cyclic-AMP, and 1 mg/mL hydrocortisone acetate. Forty μL of type I rat tail collagen (Invitrogen, Carlsbad, CA) at a concentration of 50 $\mu\text{g}/\text{mL}$ in PBS was applied to all four top channels for one hour. This surface treatment increases cell attachment. Passage 8 LECs were grown in a flask until 85% confluent. The media was removed from the flask and 4 mL of PBS was put into the flask for one minute. During this time, the flask was gently rocked to ensure the PBS touched the walls of the flask. The PBS was removed and 3 mL of trypsin was added. After 30 seconds the flask was placed in a microscope to ensure all the cells had detached. Once all of the cells detached, 7 mL of EBM was added to the flask. This solution was mixed a few times and then put into a fresh 15 mL tube and spun down at 4°C for 5 minutes. Cells were then resuspended in one mL of EBM solution and then counted with a hemocytometer. Then the LECs were seeded in the top channel of the device, refer to figure 21, by pipetting a concentration of 180,000 cell per 60 μL into a tube followed by pipetting air into the tube for exact placement of the cells in the channel. The cells were allowed to incubate and attach at 37°C and 5% CO₂ for one hour. Tubing was connected to the device and the channel was flushed with EBM. This removed any cells that were not attached to the channel, as well as supplying a larger reservoir of media to the cells. The device was then left in the incubator for at least three hours before flow experiments were performed.

3.3.2 Collagen Gel

The collagen gel was prepared on ice using 246 μL of 9.3 mg/mL collagen, 5.7 μL NaOH 1N, 4.5 μL HEPES, 45 μL PBS 10x, 150 μL deionized water, and 50 μL of the ZR75-1 cell suspension in serum-free Dulbecco's Modified Eagle Medium (DMEM). The DMEM solution consists of 20% FBS and 1% antibiotic-antimicotic mixture. 40 μL of the collagen gel was pipetted into tubing connected to the four top channels followed by pipetting air into the tubing for exact placement in the channel. It was

then allowed to polymerize in the incubator at 37°C for 15 minutes before performing flow and static experiments.

3.3.3 Dextran/Bodipy Mix

A mix of 14 mL serum free DMEM, 1 mL (10 mg/mL) fatty-acid free albumin, 15 μ L (5 mg/mL) bodipy, and 15 μ L (5 mg/mL) cascade blue dextran were mixed together. Then this solution was injected into the non-cell side for the permeability studies.

3.3.4 Flow studies

For the lipid transport/permeability study flow was incorporated in two channels onto the top side, cell side, at a flow rate of 0.175 mL/min, which corresponds to a shear stress of 0.5 *dyne/cm*², see equation 4. This solution consisted of serum-free DMEM to reduce auto-fluorescence. The previously mentioned dextran/bodipy mix was put in the non-cell side of this device to act as a source channel, while the serum-free channels acted as a sink channel for bodipy and dextran.

To produce flow in the cancer cell migration study fluid was filled to the top of the tubing inlet on one side. This corresponded to a 0.8 μ m/s velocity and an interstitial flow rate of about 0.1 μ m/s at the membrane interface. This interstitial value was calculated using a COMSOL model of the channel/membrane interface, see 39 in the results section and figures 43 and 44 in the appendix. The subdomains were set so the top channel was the cancer gel and the bottom was just media. The properties for the media were set to the dynamic viscosity and density of water at 37°C. While the density of the collagen gel was set to 9.3 mg/mL and the dynamic viscosity was 10 cP [33]. For boundary conditions, an inlet was set in the cancer gel channel at velocity of 0.8 μ m/s and the other three planes (one in the cancer gel and two in the media channel) were set to free surface pressure outlets. A very fine mesh was used and a solution was compiled.

3.4 Cell Staining

The LECs were fixed in 4% PFA at room temperature for 15 minutes. Then the channels were rinsed with PBS three times before adding DAPI for 15 minutes. The device was placed in a dark drawer during the staining process. Then the device was rinsed three times with PBS before phalloidin and staining buffer, PBS with 2% BSA, (1/100 ratio) was added for an hour. The device was again placed in a dark drawer during the staining process.

3.5 Image Processing

3.5.1 Permeability

In the permeability studies a 2.5x objective was used to take pictures every five minutes of each test section. By using this larger objective the entire top view of the x-shaped device could be seen. This was beneficial, because the concentration in both the source and sink channels could be measured. To quantify the concentration at any location a region of interest was drawn in Matlab by using the `roipoly` function. Once the region of interest was selected a mask was created and the average intensity of that region was calculated with the `mean2` function. A standard curve of intensity versus concentration was made by using this mask technique on several known concentration values. The corresponding intensity to each of these known concentrations was plot. For the experimental results, the intensity values at each time point were measured with this mask technique and then interpolated with the `interp1` function onto the standard curve and the corresponding concentration was calculated. Next, the flux was determined for both the static and flow cases This was done by calculating the exposed volume over time. Finally, the surface area is known and constant for all cases at 0.5 mm^2 . So by using equation 3 effective permeability was calculated for each case. The code for this can be found in the appendix.

3.5.2 Migration

Images were taken with a 20x objective every five minutes at a constant depth for each cross-section in the device. Over the course of three hours migration of cells can be seen, both side to side and in and out of plane. To quantify this movement two different image processing techniques were used. The first was to count the number of cells present at the very beginning and then to do a maximum intensity projection (MIP) of the entire time course to establish the number of cells that were ever present in the z slice, thus reporting the total flux in and out of this imaging plane. To do this the images were all converted to binary, in the imaging program Crystal Image (Crystal Image, Athens, GA), and a threshold was applied as well as a composite wavelet matched filter to reduce noise. Next, the channel was measured to estimate the number of pixels per length and it was determined that 100 square pixels was about the area of a cell. A watershed separation technique was used to predict and separate regions where cells could be overlapping and then a clustering technique was used to calculate how many regions were at least 100 square pixels. By doing this on both the start and projection images, the difference in number of cells indicated how many cells fluxed through the region over the course of the experiment.

The second quantification technique used the binary images and noise reduction techniques from the previous analysis, but instead performed an image subtraction. Specifically, each image was subtracted from the preceding image to establish the displacement of the individual cells during each 5 minute interval and then the average intensity of the whole region was calculated by using the Matlab function `mean2` and plotted over time, figure 41. The code for this can be found in the appendix.

CHAPTER IV

RESULTS AND DISCUSSION

4.1 Aim 1: Cell Viability

Once the device was made several experiments were performed with it. First, I needed to confirm that cells could be seeded and that they could establish healthy monolayers. There was a lot of trial and error at first due to optimizing a cell seeding protocol with the device and finding the right seeding density. I tested the following densities (45, 90, 135, 180 $\times 10^3$ cells) and found that 180,000 cells produced the best results upon visual inspection after three hours of incubation and after one day of incubation. After a few tries I found that pipetting the collagen mixture, see the methods section for a more detailed description, through a tube into my device worked best. I injected the cells in a similar manner. Before pipetting the cells into the device, I would gently mix the cell solution to ensure the cells were evenly distributed and would then slowly pipette the solution into the tube, followed by slowly pipetting air into the tube to get exact placement of the cell solution in the channel. I found that a seeding density of 180,000 cells per 60 μL produced evenly distributed cells throughout my channels. After incubating the cells for three hours I would also have confluent, healthy monolayers, at which point a cancer gel could be injected and/or flow experiments could be performed.

After the flow experiments, LECs were fixed and stained with dapi and phalloidin to visual the nucleus and actin filaments. Note, the cancer cells were stained with a live cell stain that fluoresces in the rhodamine channel so phalloidin that fluoresces in the GFP channel had to be used on the LECs with the cancer gel co-culture. Whereas, phalloidin that fluoresces in the rhodamine channel was used on the permeability

studies.

Figure 27 shows the LECs from the cancer gel co-culture. Again, blue shows the nucleus of the LECs and the green are the actin filaments. In these particular images, the cells were seeded on 8 μm pore sized membranes. Even though the pore size is quite large, the cells are still about 90% confluent. This pore size was chosen for the cancer cells to be able to migrate through the membrane and endothelial layer. Another important feature from these images is the even distribution of cells. This is quite important, because inadequate cell densities can cause the LECs to start differentiating, which would be highly undesirable.

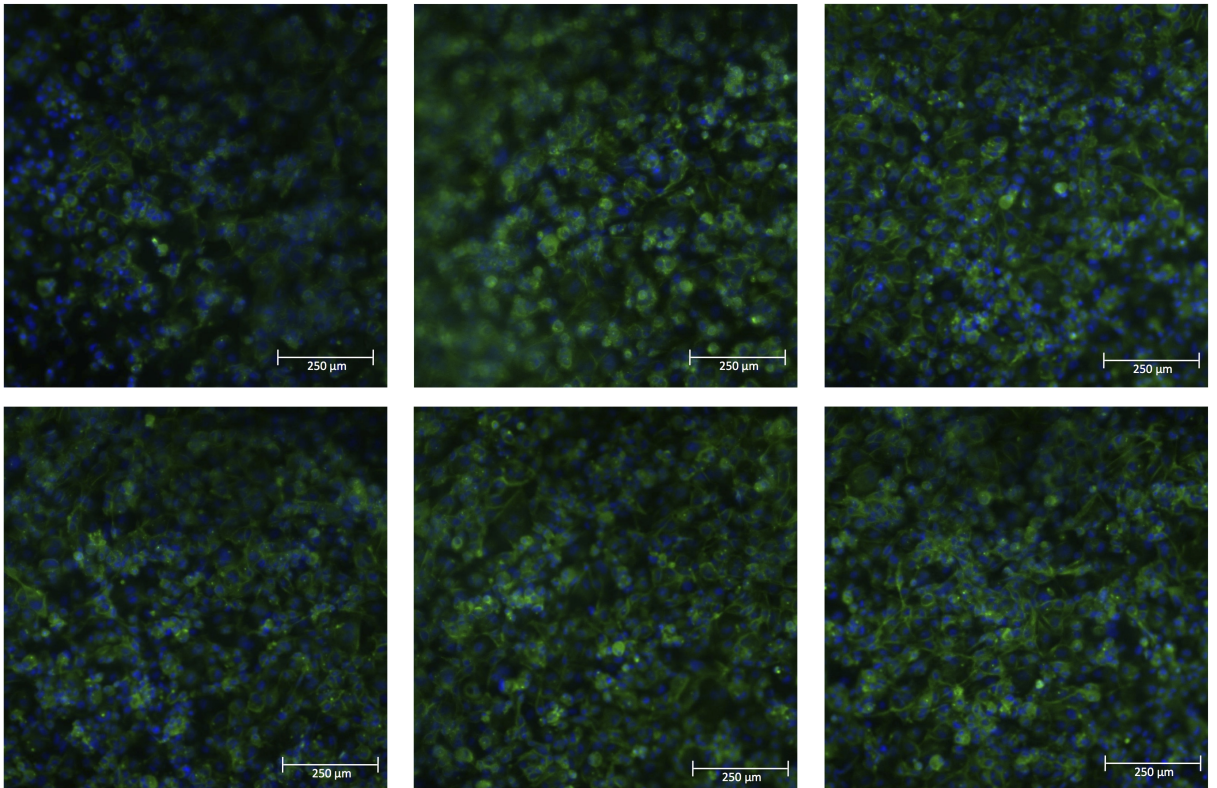


Figure 27: LECs stained with dapi and phalloidin

Now, figure 28 shows an overlay of dapi, GFP, rhodamine, and the bright field channel. In this case, dapi is again used to show the nucleus of the LECs, green phalloidin shows the actin filaments, rhodamine shows the live cell dye of the cancer

cells, and bright field shows the membrane. What is really interesting about these images is the red tinge to the whole image. The camera was focused on the membrane at the LEC layer, as shown by bright field and the LEC stains, but the cancer cells can still be faintly seen in the background. The washed out appearance of the red throughout the image indicates that the cancer cells are out of focus, as expected, but also shows their presence. These images really highlight the potential for co-cultures in this device as well as incite promising future experiments. For instance, if the LECs could also have a live cell stain really interesting images could be taken during static and flow experiments. You should be able to capture an image of a cancer cell migrating through the LEC layer, as has been shown previously in fixed samples [37].

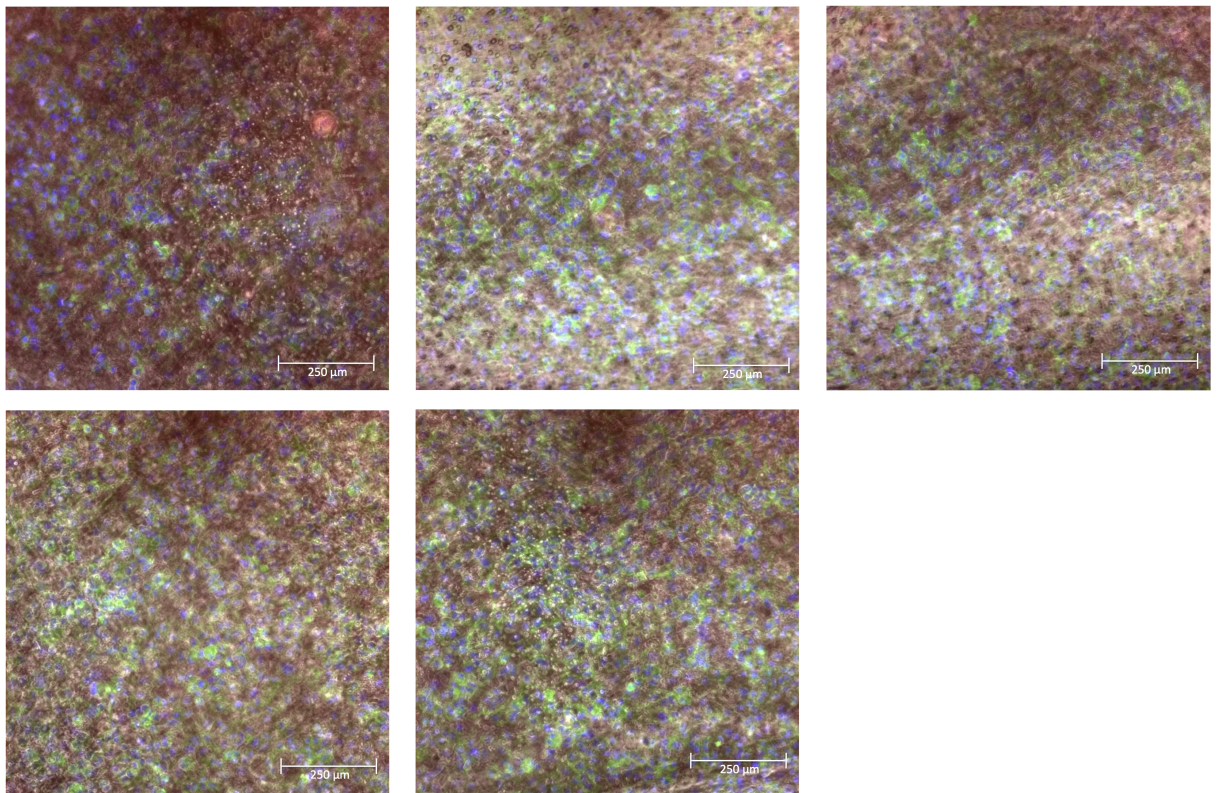


Figure 28: Co-culture of cancer cells with LECs

One challenge associated with fixing and staining the LECs is that the live cell stain of the cancer cells severely diminishes upon fixation. This could be overcome by

restaining the cancer cells and their nuclei with dapi and with a cell-specific antibody. Figure 29 shows images of the LECs just stained with dapi and the cancer cells in the background. At this point, 30 minutes had passed since the 4% PFA had been introduced to the system. The difference in the intensity of the cancer cells between these images and the previous figure are significant. Note, phalloidin takes an hour so the images in figure 28 were taken at least an hour and half since the 4% PFA had been introduced.

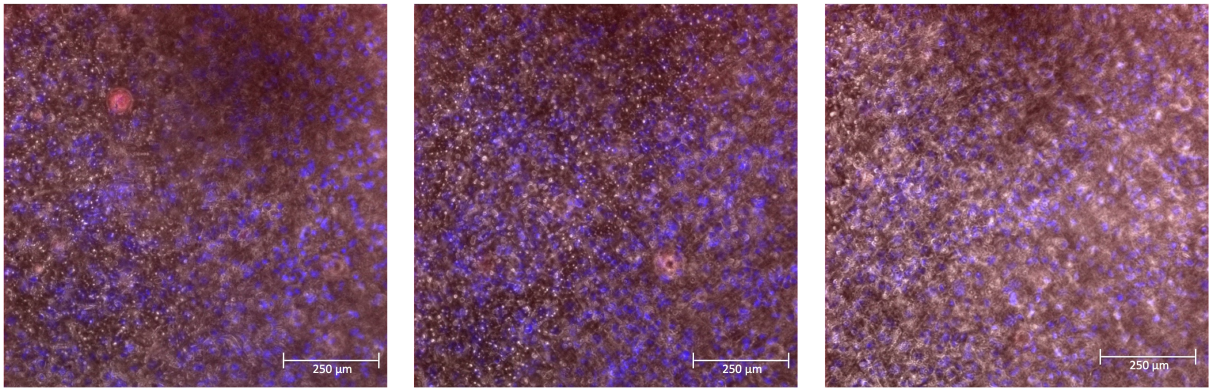


Figure 29: Co-culture with just dapi and rhodamine channels

Cancer cells can also be cultured independent of LECs as shown in figure 30. The live cell stain does a good job at highlighting the cancer cells. These images also show how evenly distributed the cancer cells are in the gel from side to side as well as hinting at the distribution in the plane. Several cells can be seen just out of field.

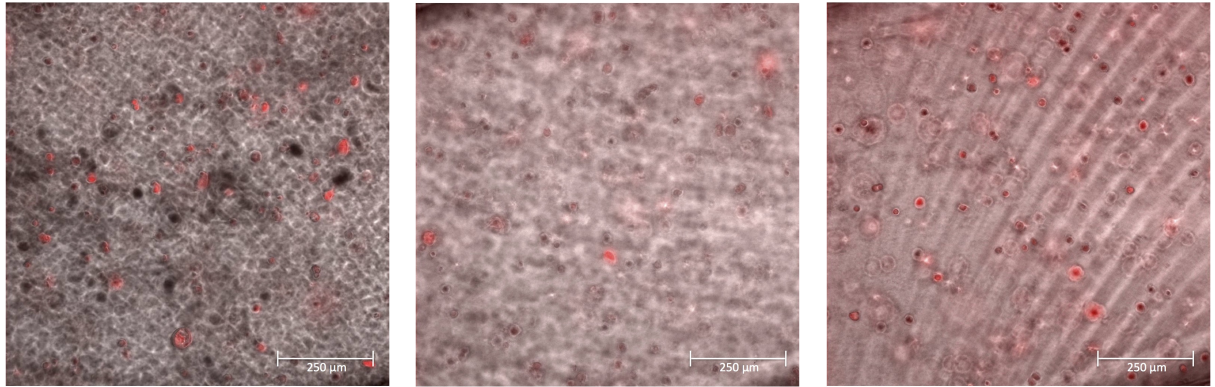


Figure 30: Bright field image of cancer cells with live cell dye

The final set of images are from the permeability studies, see figure 31. In these images dapi and red phalloidin were used to again show the nucleus and actin filaments. The cells are evenly distributed and about 85% confluent. Unfortunately, the phalloidin stain is much harder to see than in the previous images. This is primarily due to the integration time being too low. Unfortunately, the green phalloidin cannot be used in this case due to the bodipy solution that is applied during the flow experiments. The channels still fluoresce very intensely even once the bodipy has been removed from the channel and the channel has been rinsed several times with PBS. Figure 32 even shows bodipy deposits near the cells. Bodipy deposits are indicators of lipid uptake. During the static and flow permeability studies, these deposits can be seen in real time, meaning that bodipy is being taken up throughout the experiment.

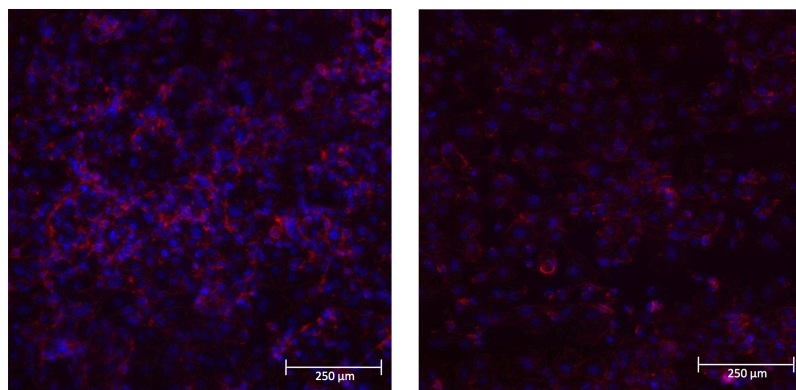


Figure 31: LECs stained with dapi and phalloidin

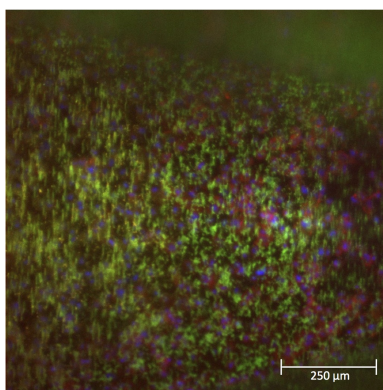


Figure 32: LECs stained with dapi and phalloidin with bodipy deposits

Overall, cells can be seeded on this device and kept alive while varying different experimental conditions.

4.2 Aim 2: Permeability

If we recall from chapter 2, figure 5 shows a model that could be used for drug screening, lipid uptake, or lymphedema studies. To establish that this model could be used for studying lipid transport in any of these cases, permeability will be measured in a static case and in a flow case, 0.175 mL/min ($1/2$ dyne/cm²). We are measuring effective permeability because it quantifies the transport of a particular molecule across a surface. In this case, fluorescently labeled dextran and bodipy will be used,

because dextran is a standard molecule used for characterizing passive permeability and bodipy is used to quantify lipid uptake.

Permeability

$$P_{eff} = \frac{J_s}{\Delta CS} \quad (5)$$

is influenced by flux, concentration, and surface area. Based on the designed system, the exposed surface area of the membrane is constant at 0.5 mm^2 . This leaves flux and concentration which are both conditional. Flux varies with the concentration of the tracer and exposed volume over time, which means the value was significantly higher in the flow case. For the flow case, flux is equal to the concentration multiplied by the flow, 0.0029 mL/s (0.175 mL/min), as compared to the static case where flux is equal to the concentration multiplied by the exposed volume over the time course, $6.4 \times 10^{-6} \text{ mL/s}$ ($23 \text{ } \mu\text{L/hr}$). Just from these values we know that the flow case will have a much higher effective permeability simply due to convection. This is because the sink channel is being constantly diluted which means the concentration gradient will larger than in the static case. Which further emphasizes how important flow is to incorporate in lymphatic biology. It plays a huge role in inflammation and normal fluid homeostasis and just from the effective permeability equation we can see how important flux is on permeability.

The final value needed to find permeability is the concentration of the probe that has been transported to the apical side of the lymphatics. Known concentration of bodipy and dextran were put in the channel and images were taken of each. Then the average intensity was found of that channel, see figure 33. Finally a standard curve, see figure 34, was made for both bodipy and dextran by plotting concentration versus average intensity.

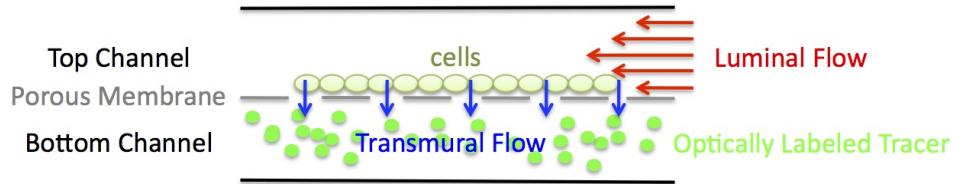


Figure 33: Region of interest used in channels

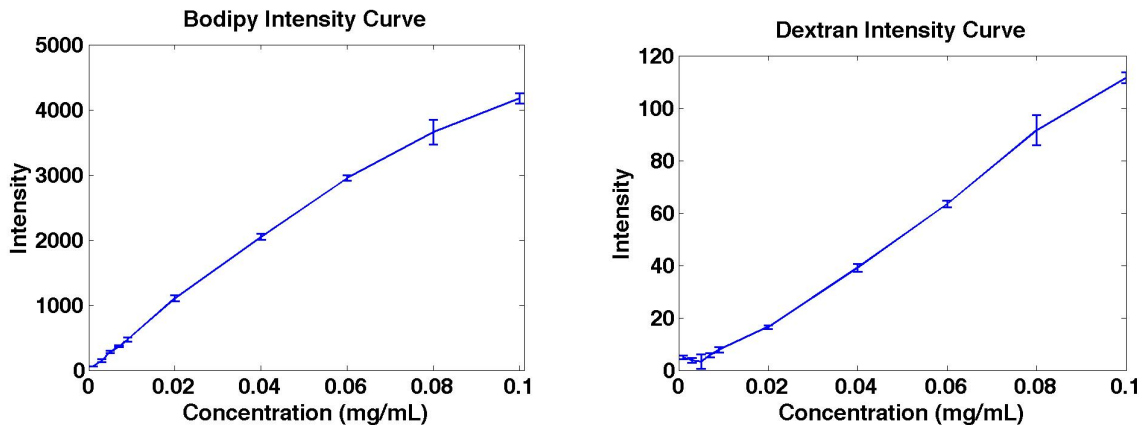


Figure 34: Intensity vs Concentration for bodipy (left) and dextran (right)

Concentrations of fluorescently labeled bodipy and dextran were added to the bottom channel of the device, see figure 35. This channel corresponds to the no cell and no flow channel. By putting the fluorescently labeled molecules in the no cell and no flow channel the uptake into the lymphatics when vessel leaking is occurring could be represented. If the solution was added to the cell and flow side instead, one could quantify just vessel leakage. While both of these configurations have a purpose, the uptake model was chosen simply because we know from chapter 2 that flow increases the transport and uptake of lipids into lymphatics. Whereas, the other configuration would just describe how leaky the system is.

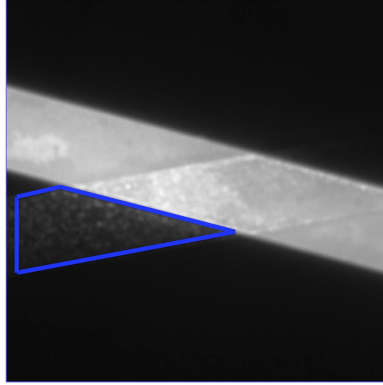


Figure 35: Flow model with optically labeled tracer in bottom channel

Once the average intensity of the channel show in figure 35 had been calculated it was interpolated on to the previously mentioned standard curve to establish the corresponding concentration. Finally, the difference in concentration from the initial and final images was calculated.

Table 8 and figure 36 shows the progression of dextran in both the static and flow cases. The image sequences show the initial image and then after 20, 35, and 50 minutes. For each of these cases, the effective permeability was calculated for the duration of the experiment. In the static case, the average $P_{eff}=0.003 \mu\text{m/s}$ and in the flow case $P_{eff}=0.126 \mu\text{m/s}$. The static case permeability is less than the value found by Dixon et al. in transwells, $0.065 \mu\text{m/s}$ [13]. The difference could be due to different concentrations used. An important parameter to note is that flow is recirculating in the sink channel of the flow case. So while it is not illuminating as strongly as the static case, it is being spread over a much larger amount of fluid and has a much larger fluid flux. This could be potentially problematic. While the solution does eventually illuminate the time required to do so is much higher than in the static case.

Table 8: Flow increases effective permeability of Dextran

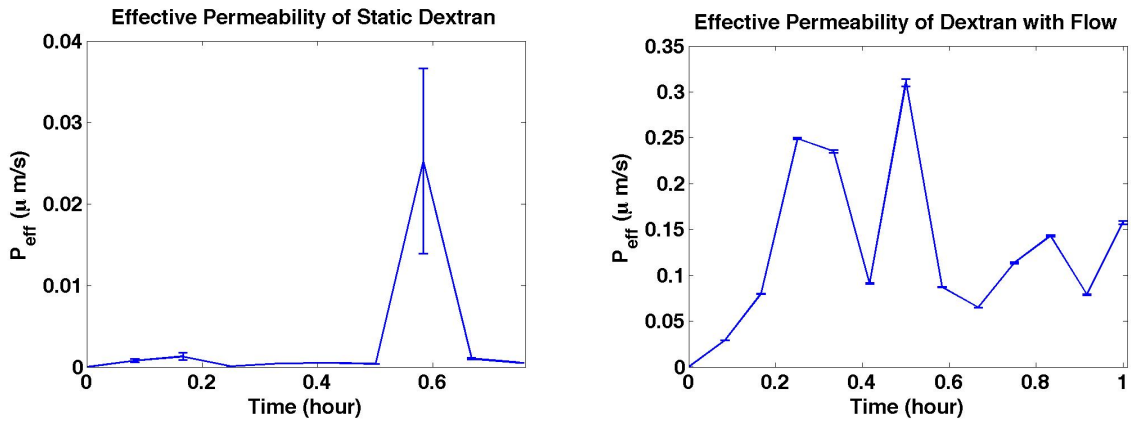
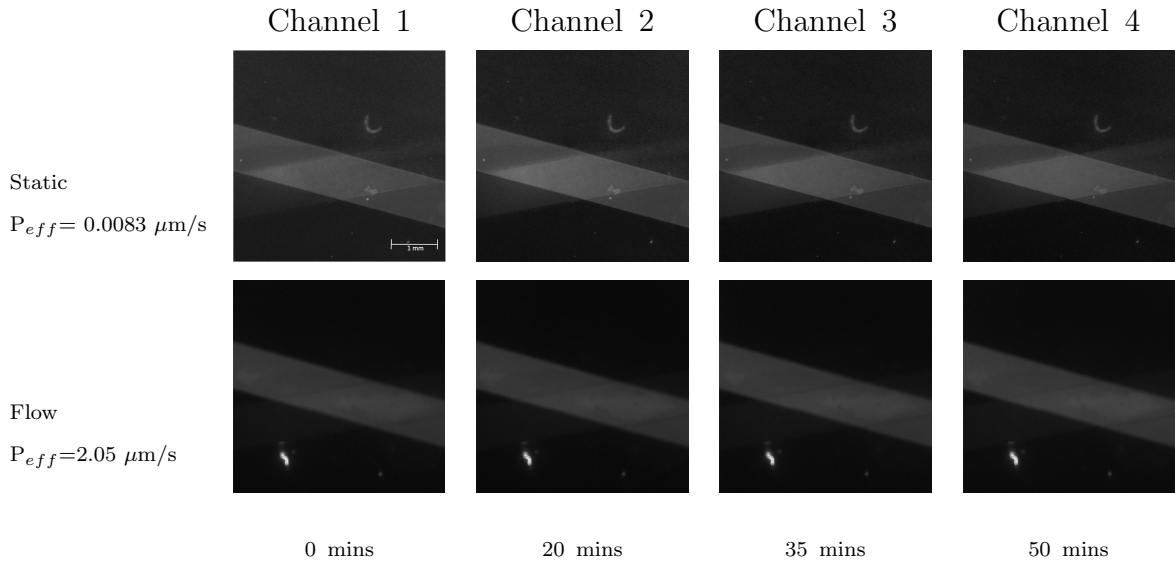


Figure 36: Dextran permeability throughout experiment for static (left) and flow cases (right)

Table 9 and figure 37 also show the progression in the static and flow cases, but of bodipy. What's interesting in the bodipy case is the accumulation of bodipy deposits in the cell layer. The deposits appear more frequently and in a higher quantity for the flow case which corresponds to increase in lipid uptake when flow is present [60]. These bodipy deposits appear as small dots in the sink channel and because of this it is much easier to see the increased uptake of bodipy in the flow case. The

calculated effective permeability is, as expected, much higher in the flow case. Where the static case $P_{eff}=0.002 \mu\text{m/s}$ and in the flow case $P_{eff}=0.12 \mu\text{m/s}$. The static case permeability corresponds very closely with the value found by Dixon et al. of $0.005 \mu\text{m/s}$ [13]. These bodipy deposit regions can affect the permeability calculation though, because the measured concentration of the solution will be increased when these deposits are available.

Table 9: Flow increases effective permeability of Bodipy

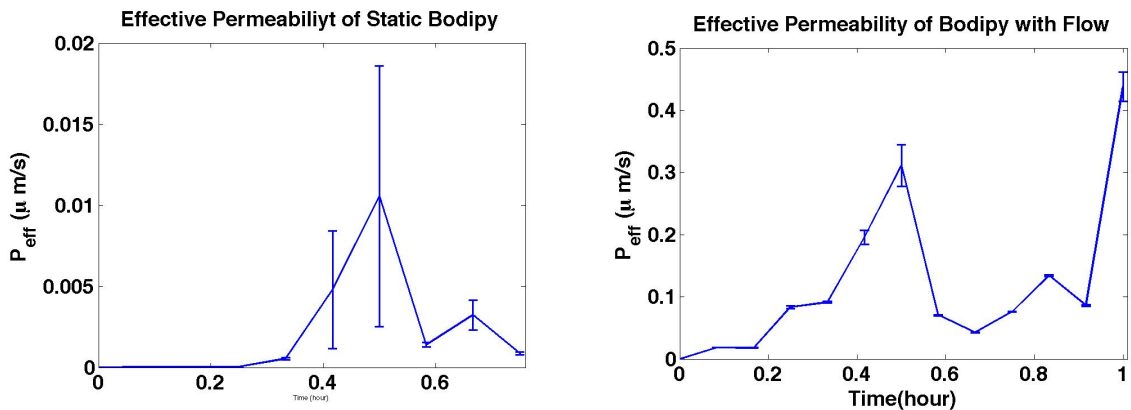
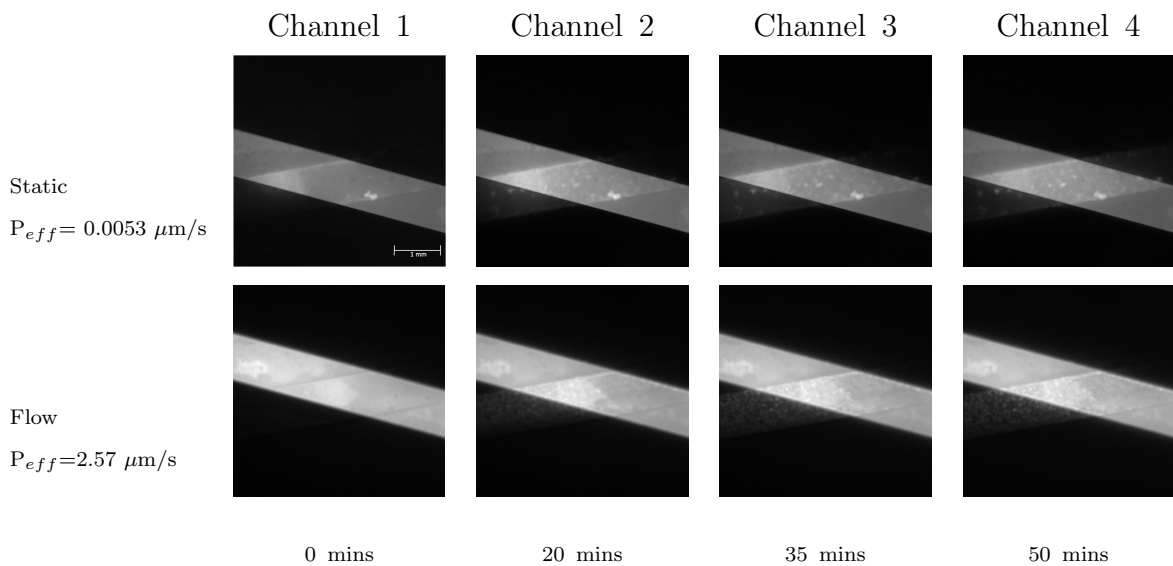


Figure 37: Bodipy permeability throughout experiment for static (left) and flow cases (right)

4.3 Aim 3: Migration

As mentioned in chapter 2, a model that shows migration through a tumor like structure (collagen gel) into the lymphatics is useful for studying cancer cell homing mechanisms to the lymphatics. In this model, see figure 6, cancer cells can be imaged at multiple time intervals which allows for quantifying motility of cancer cells in the collagen gel.

4.3.1 Interstitial Flow in Cancer Gel

Before delving into the quantification of migration, the interstitial flow rate through the membrane of the cancer gel case needed to be calculated. This ensures that biophysically relevant flows, 0.1 to 0.8 $\mu\text{m/s}$ [52], are acting on the cancer cells. To determine what the interstitial flow rate through the membrane, the flow rate entering the gel channel was determined experimentally and then the input into a COMSOL model.

Fluid was filled to the top of the tube holder column, see figure 38, and then after 12 hours the height of the fluid still in the column was measured. The fluid had moved down half of the length of the tube column, 0.1 inches, and the diameter of the column is 1/8 inch. Taking this displaced volume over the time and then dividing by the channel cross-sectional area resulted in a velocity of 0.8 $\mu\text{m/s}$. Media was only filled in one column to establish a hydrostatic pressure gradient to drive flow through the cancer gel.

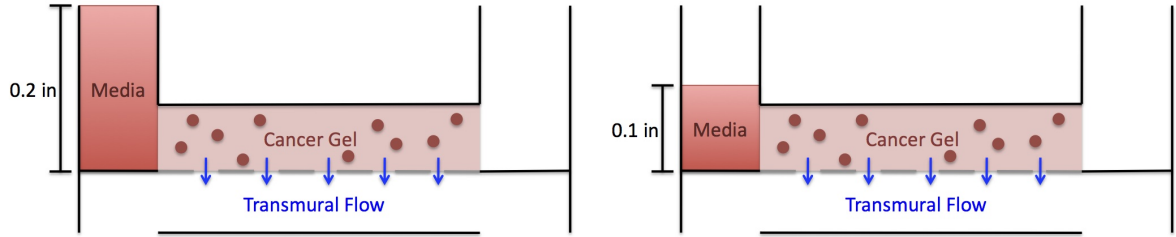


Figure 38: Initial height of media added to channel (left) and final height after 12 hours (right)

A COMSOL model was created where the top channel was the cancer gel and the bottom was just media. The properties for the media were set to the dynamic viscosity and density of water at 37°C. While the density of the collagen gel was set to 9.3 mg/mL and the dynamic viscosity was 10 cP [33]. Figure 39 shows the side view of the cross section and the isometric view of the channels. From figure 39 (left), a range of 0 to 0.1 μm was set to distinguish the flow rate in the bottom channel and we can see that the interstitial flow from the total velocity is around 0.1 $\mu\text{m/s}$ at the membrane interface, top of the colored rectangle, which is within the range for acceptable interstitial flow.

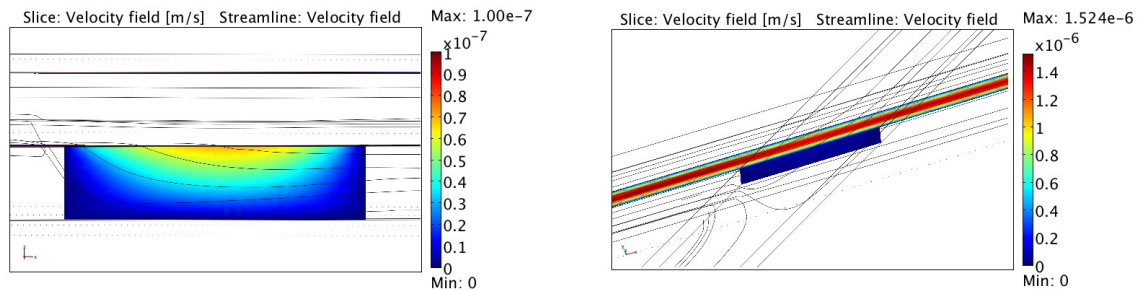


Figure 39: Side view of cross-sectional area (left) and isometric view of model (right)

4.3.2 Migration

ZR75-1 breast cancer cells were used in initial cancer migration studies, because they were previously shown to have the strongest migratory response to flow and are known to be highly metastatic [52]. The microscope was focused to a depth just above the membrane in the collagen gel where cancer cells were present. This z slice depth was used for all of the channels. Images were then taken every five minutes with the rhodamine filter to capture the live cell dye on the cancer cells. This was done in three channels, where one was static and the other two were with flow.

By only inducing flow through one column, flow through the gel occurs from left to right as well as transmurally. To avoid this in the future both columns could be filled with media to drive transmural flow.

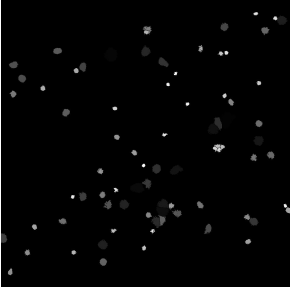


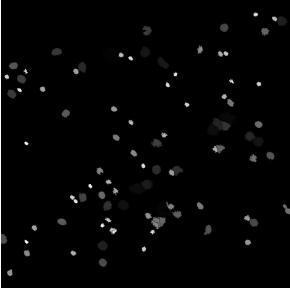
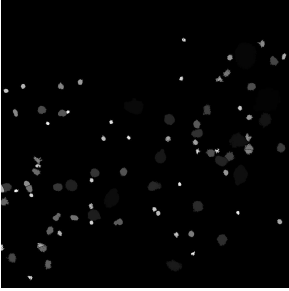
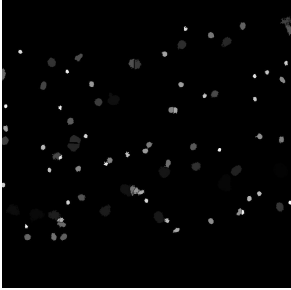
Two different imaging techniques were used to quantify cancer cell migration through this z slice. The first shows cell flux through this z slice and the second shows cell motility.

4.3.2.1 Cell Flux

All collected images were binarized, thresholded to reduce noise, smoothed out with a composite wavelet matched filter, and areas that were close to one another were separated with a watershed technique to ensure any cells that were close to one another were separated. Then a clustering technique was used to determine the number of regions that were at least 100 square pixels. Where 100 square pixels is about the minimum size of a cell. This clustering technique was used on the initial image to establish the number of cells that were present to begin with. Then a maximum intensity projection (MIP) was created by compressing all of the images from the experiment into a single image that showed the presence of any cell that had existed in the z slice throughout the experiment. The clustering technique was used on the MIP to establish the number of cells that had ever been present in the

z slice during the experiment. Table 10 shows the initial images and MIP images for the static and two flow cases.

Table 10: Cell flux through collagen gel z slice

	Static	Flow 1	Flow 2
Initial			
MIP			
Difference	15	24	40
Percentage of Change	19%	37.5%	88.9%

The static channel started with 79 cells and overall it had 94 cells present in that z slice. Which indicates that at least 15 additional cells moved from the beginning of the experiment to the end. Next, the first flow channel started with 64 cells and overall it had 88 cells for an overall change of 24 cells. Last the second flow channel started with 45 cells and overall it had 85 cells for a difference of 40 cells. While both the flow channels had a larger difference in cells present, there is not enough evidence in this model, yet, to establish a correlation between flow and cancer cell migration, but the data suggests that the presence of flow increases cell migration which corresponds to Shields et al. [52]. More experiments will need to be performed. This quantification is useful for establishing the flux of cells through a z slice during a time course and it

is a more accurate count of the number of cells present during the experiment than the end-point count performed by Shields et al. though.

4.3.2.2 Cell Motility

As mentioned previously, a second technique was used to quantify cell motility. The same images were used for both techniques, however, instead of counting the number of regions that were large enough to be a cell the changes between time points was calculated. To do this, each image had the previous image in the sequence subtracted from it. For example, the fifth image captured would have the fourth image subtracted from it. By doing this, the remaining image would show any changes that happened to the cell locations between the time points in either depth or from side to side. Figure 40 shows a subtracted image from the flow 1 channel. In this image two types of movement can be seen. The first is the ring formed by changes in depth from coming into and out of focus. While the second are crescents formed from side to side movement.

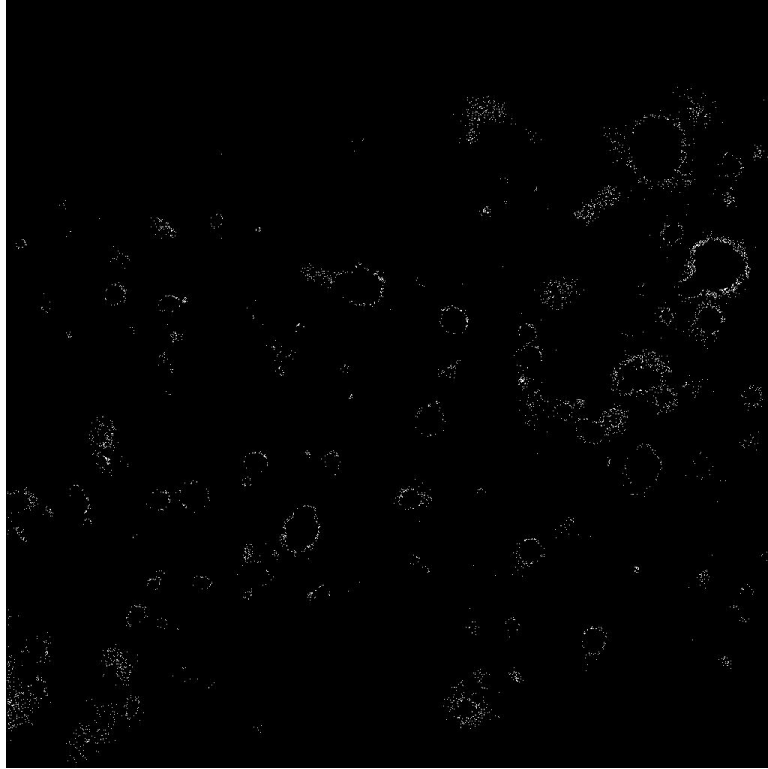


Figure 40: Resulting image from subtraction

The average intensity was taken of each of these subtracted images and plot versus time, see figure 41. In this graph we see that static, flow 1 and flow 2 move at about the same frequency which suggests cancer cells have the same motility regardless of the presence of flow. The interesting trend is in the flow 2 case where the magnitude and frequency of changes is relatively low in comparison to the other channels. Upon inspection of the subtracted images, cells moved primarily in and out of focus in this channel as opposed to moving from side to side. The intensity due to variations in direction cannot be distinguished from the intensity due to the number of cells present so directionality cannot be determine on its own. Also, the peaks happen fairly regularly for the static and flow cases, this suggests that the flow case is just as motile as the static case. What is most interesting question from this finding is, if the cells are just as motile in the static case as the flow case then why do more cells flux through the z slice as shown in the previous section? This further emphasizes the

importance of including flow in migration models as it most likely is directing cancer cell migration into the lymphatics.

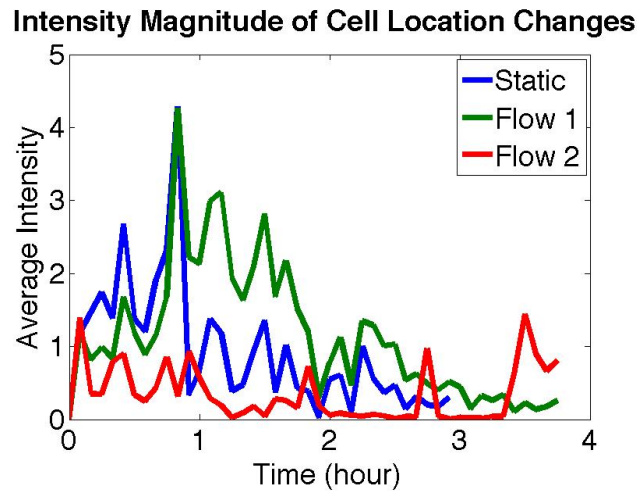


Figure 41: Magnitude and frequency of movement changes

Overall, these two techniques may allow for quantification of cell flux as well as show the motility of cells in this device. More experiments need to be performed, but these initial findings are an indicator that flow could have profound effects on migration into lymphatics.

CHAPTER V

CONCLUSION

5.1 Conclusion

With this device, I have shown that cells can be cultured on both membranes and in collagen gels and are viable during experiments. I can induce both luminal and transmural flow through this device and clear images of the channels can be taken. I have demonstrated the possibility to calculate the effective permeability of two fluorescently labeled transport molecules in both static and flow conditions. I have presented potential quantification methods for measuring cell migration in real time that shows both motility and flux of the cells which may be applied to further studying cancer cell homing mechanisms into the lymphatics. Overall, this device addresses all the designated aims in chapter 2, as well as sets the foundation for future studies in both lipid transport and cancer cell migration.

5.1.1 Future Work

5.1.1.1 Lipid Transport

This device will be used to answer the following two questions.

How are lipid uptake mechanisms affected by transmural flow?

How is permeability affected by varying shear stress and by oscillatory luminal flow?

The first will help in studying the fundamental mechanisms involved with lipid uptake and could be beneficial in progress towards drug delivery through lymphatics. The second would be useful for establishing how flow influences permeability and lipid uptake due to changes in flow patterns as well as shear stress.

5.1.1.2 Cancer Metastasis

For the cancer model, there are also two questions of interest.

How does the presence of lipoproteins affect cancer cell migration?

How is cancer cell migration affected by luminal flow across the LEC layer?

Hyperlipidemia patients have been shown to have favorable circumstance for cancer growth [31] so the main point of the first question is to see if these additional lipoproteins influence cancer cell migration in any way. The migration quantification methods shown in this thesis will prove to be very useful for answering this question. The second, as shown in figure 42, luminal flow would be induced across a LEC layer which should increase the CCL19/21 concentration gradient and cause an even more profound migration of cancer cells to the LECs. Where the pressure gradient through the membrane formed by the flow through the collagen gel would be greater than the pressure gradient through the membrane caused by the luminal flow.

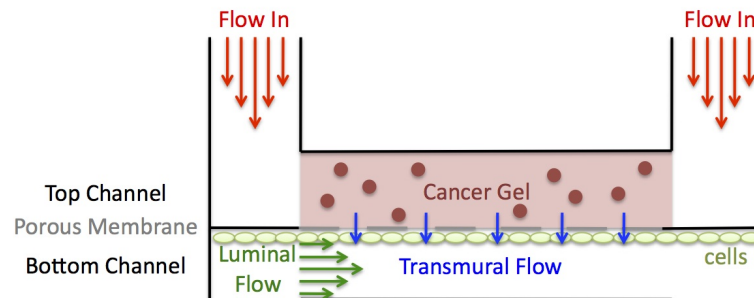


Figure 42: Cancer cells suspended in collagen gel with luminal flow on LEC side

APPENDIX A

MATLAB CODE

Region of interest code for concentration curve:

```
close all
clear all
clc

%Standard Intensity Curve
%Background Dextran
files = dir('Background/Dextran/*.TIF'); %Finds all tif files in folder
num_files = numel(files); %Finds number of images
Look = dir('Background/Dextran/*.jpg'); %Finds jpg
a=imread(Look(1).name); %Reads image
mask=roipoly(a); %Create ROI mask
close %Close window
for k = 1:num_files %Loop through all images
    a=imread(files(k).name); %Read in image
    b(k)=mean2(a(mask)); %Average intensity of mask on
each image
end
c1=mean(b); %Average over set

%Dextran 001
files = dir('001/Dextran/*.TIF'); %Finds all tif files in folder
num_files = numel(files); %Finds number of images
for k = 1:num_files %Loop through all images
    a=imread(files(k).name); %Read in image
    b(k)=mean2(a(mask)); %Average intensity of mask on
each image
end
Ed1=std(b); %Standard Deviation
cD1=mean(b-c1); %Average over set

%Dextran 003
files = dir('003/Dextran/*.TIF'); %Finds all tif files in folder
num_files = numel(files); %Finds number of images
for k = 1:num_files %Loop through all images
    a=imread(files(k).name); %Read in image
    b(k)=mean2(a(mask)); %Average intensity of mask on
each image
end
Ed3=std(b); %Standard Deviation
cD3=abs(mean(b-c1)); %Average over set

%Dextran 005
files = dir('005/Dextran/*.TIF'); %Finds all tif files in folder
num_files = numel(files); %Finds number of images
for k = 1:num_files %Loop through all images
    a=imread(files(k).name); %Read in image
    b(k)=mean2(a(mask)); %Average intensity of mask on
each image
end
Ed5=std(b); %Standard Deviation
cD5=mean(b-c1); %Average over set

%Dextran 007
files = dir('007/Dextran/*.TIF');
```

```

num_files = numel(files);
for k = 1:num_files
    a=imread(files(k).name);
    b(k)=mean2(a(mask));
end
Ed7=std(b);
cD7=mean(b-c1);

%Dextran 009
files = dir('009/Dextran/*.TIF');
num_files = numel(files);
for k = 1:num_files
    a=imread(files(k).name);
    b(k)=mean2(a(mask));
end
Ed9=std(b);
cD9=mean(b-c1);

%Dextran 02
files = dir('02/Dextran/*.TIF');
num_files = numel(files);
for k = 1:num_files
    a=imread(files(k).name);
    b(k)=mean2(a(mask));
end
Ed20=std(b);
cD20=mean(b-c1);

%Dextran 04
files = dir('04/Dextran/*.TIF');
num_files = numel(files);
for k = 1:num_files
    a=imread(files(k).name);
    b(k)=mean2(a(mask));
end
Ed40=std(b);
cD40=mean(b-c1);

%Dextran 06
files = dir('06/Dextran/*.TIF');
num_files = numel(files);
for k = 1:num_files
    a=imread(files(k).name);
    b(k)=mean2(a(mask));
end
Ed60=std(b);
cD60=mean(b-c1);

%Dextran 08

```

%Finds number of images
 %Loop through all images
 %Read in image
 %Average intensity of mask on

 %Standard Deviation
 %Average over set

 %Finds all tif files in folder
 %Finds number of images
 %Loop through all images
 %Read in image
 %Average intensity of mask on

 %Standard Deviation
 %Average over set

 %Finds all tif files in folder
 %Finds number of images
 %Loop through all images
 %Read in image
 %Average intensity of mask on

 %Standard Deviation
 %Average over set

 %Finds all tif files in folder
 %Finds number of images
 %Loop through all images
 %Read in image
 %Average intensity of mask on

 %Standard Deviation
 %Average over set

 %Finds all tif files in folder
 %Finds number of images
 %Loop through all images
 %Read in image
 %Average intensity of mask on

 %Standard Deviation
 %Average over set

 %Finds all tif files in folder
 %Finds number of images
 %Loop through all images
 %Read in image
 %Average intensity of mask on

 %Standard Deviation
 %Average over set

```

files = dir('08/Dextran/*.TIF');
num_files = numel(files);
for k = 1:num_files
    a=imread(files(k).name);
    b(k)=mean2(a(mask));
end
Ed80=std(b);
cD80=mean(b-c1);

%Dextran 1
files = dir('1/Dextran/*.TIF');
num_files = numel(files);
for k = 1:num_files
    a=imread(files(k).name);
    b(k)=mean2(a(mask));
end
Ed100=std(b);
cD100=mean(b-c1);

%Background Bodipy
files = dir('Background/Bodipy/*.TIF');
num_files = numel(files);
Look2 = dir('Background/Bodipy/*.jpg');
a=imread(Look2(1).name);
mask=roipoly(a);
close
for k = 1:num_files
    a=imread(files(k).name);
    b(k)=mean2(a(mask));
end
c2=mean(b);

%Bodipy 001
files = dir('001/Bodipy/*.TIF');
num_files = numel(files);
for k = 1:num_files
    a=imread(files(k).name);
    b(k)=mean2(a(mask));
end
Eb1=std(b);
cB1=mean(b-c2);

%Bodipy 003
files = dir('003/Bodipy/*.TIF');
num_files = numel(files);
for k = 1:num_files
    a=imread(files(k).name);
    b(k)=mean2(a(mask));
end

```

```

%Finds all tif files in folder
%Finds number of images
%Loop through all images
%Read in image
%Average intensity of mask on

%Standard Deviation
%Average over set

%Finds all tif files in folder
%Finds number of images
%Loop through all images
%Read in image
%Average intensity of mask on

%Standard Deviation
%Average over set

%Finds all tif files in folder
%Finds number of images
%Finds jpg
%Reads image
%Create ROI mask
%Close window
%Loop through all images
%Read in image
%Average intensity of mask on

%Average over set

%Finds all tif files in folder
%Finds number of images
%Loop through all images
%Read in image
%Average intensity of mask on

%Standard Deviation
%Average over set

%Finds all tif files in folder
%Finds number of images
%Loop through all images
%Read in image
%Average intensity of mask on

```

```

Eb3=std(b); %Standard Deviation
cB3=mean(b-c2); %Average over set

%Bodipy 005
files = dir('005/Bodipy/*.TIF'); %Finds all tif files in folder
num_files = numel(files); %Finds number of images
for k = 1:num_files %Loop through all images
    a=imread(files(k).name); %Read in image
    b(k)=mean2(a(mask)); %Average intensity of mask on
each image
end
Eb5=std(b); %Standard Deviation
cB5=mean(b-c2); %Average over set

%Bodipy 007
files = dir('007/Bodipy/*.TIF'); %Finds all tif files in folder
num_files = numel(files); %Finds number of images
for k = 1:num_files %Loop through all images
    a=imread(files(k).name); %Read in image
    b(k)=mean2(a(mask)); %Average intensity of mask on
each image
end
Eb7=std(b); %Standard Deviation
cB7=mean(b-c2); %Average over set

%Bodipy 009
files = dir('009/Bodipy/*.TIF'); %Finds all tif files in folder
num_files = numel(files); %Finds number of images
for k = 1:num_files %Loop through all images
    a=imread(files(k).name); %Read in image
    b(k)=mean2(a(mask)); %Average intensity of mask on
each image
end
Eb9=std(b); %Standard Deviation
cB9=mean(b-c2); %Average over set

%Bodipy 02
files = dir('02/Bodipy/*.TIF'); %Finds all tif files in folder
num_files = numel(files); %Finds number of images
for k = 1:num_files %Loop through all images
    a=imread(files(k).name); %Read in image
    b(k)=mean2(a(mask)); %Average intensity of mask on
each image
end
Eb20=std(b); %Standard Deviation
cB20=mean(b-c2); %Average over set

%Bodipy 04
files = dir('04/Bodipy/*.TIF'); %Finds all tif files in folder
num_files = numel(files); %Finds number of images
for k = 1:num_files %Loop through all images
    a=imread(files(k).name); %Read in image
    b(k)=mean2(a(mask)); %Average intensity of mask on
each image

```



```

end
Eb40=std(b); %Standard Deviation
cB40=mean(b-c2); %Average over set

%Bodipy 06
files = dir('06/Bodipy/*.TIF'); %Finds all tif files in folder
num_files = numel(files); %Finds number of images
for k = 1:num_files %Loop through all images
    a=imread(files(k).name); %Read in image
    b(k)=mean2(a(mask)); %Average intensity of mask on
each image
end
Eb60=std(b); %Standard Deviation
cB60=mean(b-c2); %Average over set

%Bodipy 08
files = dir('08/Bodipy/*.TIF'); %Finds all tif files in folder
num_files = numel(files); %Finds number of images
for k = 1:num_files %Loop through all images
    a=imread(files(k).name); %Read in image
    b(k)=mean2(a(mask)); %Average intensity of mask on
each image
end
Eb80=std(b); %Standard Deviation
cB80=mean(b-c2); %Average over set

%Bodipy 1
files = dir('1/Bodipy/*.TIF'); %Finds all tif files in folder
num_files = numel(files); %Finds number of images
for k = 1:num_files %Loop through all images
    a=imread(files(k).name); %Read in image
    b(k)=mean2(a(mask)); %Average intensity of mask on
each image
end
Eb100=std(b); %Standard Deviation
cB100=mean(b-c2); %Average over set

cB=[cB1,cB3,cB5,cB7,cB9,cB20,cB40,cB60,cB80,cB100]; %Bodipy values
cD=[cD1,cD3,cD5,cD7,cD9,cD20,cD40,cD60,cD80,cD100]; %Dextran values

conc=[0.001, 0.003, 0.005, 0.007, 0.009, 0.02, 0.04 0.06, 0.08, 0.1];
%Concentration values

Ed=[Ed1,Ed3,Ed5,Ed7,Ed9,Ed20,Ed40,Ed60,Ed80,Ed100]; %Standard Deviations
Dextran
Eb=[Eb1,Eb3,Eb5,Eb7,Eb9,Eb20,Eb40,Eb60,Eb80,Eb100]; %Standard Deviations
Bodipy

%Plot errorbar graphs for Bodipy and Dextran
figure()
errorbar(conc,cB,Eb)

figure()
errorbar(conc,cD,Ed)

```

Region of interest code for permeability studies:

```

close all
clear all
clc

S=0.5;

%Standard Curve Values
cB=[0 61.8 149.9 286.9 368 478.9 1132.2 2078.8 2978.1 3705.3 4224.1];
%Bodipy Values from Intensity
cD=[4.9507 3.7891 3.3300 5.7697 7.7725 16.4812 39.0864 63.4297 91.5546
111.6085]; %Dextran Values from Intensity
conc=[0.001, 0.003, 0.005, 0.007, 0.009, 0.02, 0.04 0.06, 0.08, 0.1];
%Concentration values
concB=[0 0.001, 0.003, 0.005, 0.007, 0.009, 0.02, 0.04 0.06, 0.08, 0.1];

%Permeability-Concentration (mg/mL)
%Flow
%Bodipy
files = dir('Flow Transport/Channel 1/Bodipy/Jpeg/*.jpg'); %Finds all tif
files in folder
num_files = numel(files); %Finds number of
images %Time between
t1=(0:300:300*(num_files-1))/3600;
each image
a=imread(files(1).name); %Read in image
mask1=roipoly(a); %Create ROI mask
mask2=roipoly(a);
mask3=roipoly(a);
close %Close window
for k = 1:num_files %Loop through all
images
a=imread(files(k).name); %Read in image
bF1(k)=mean2(a(mask1)); %Average
intensity of mask on image
bF2(k)=mean2(a(mask2));
bF3(k)=mean2(a(mask3));
q1_1(k)=interp1(cB,concB,bF1(k)); %Concentration
q1_2(k)=interp1(cB,concB,bF2(k));
q1_3(k)=interp1(cB,concB,bF3(k));
J_bF1(k)=q1_1(k)*0.0029; %Flux
J_bF2(k)=q1_2(k)*0.0029;
J_bF3(k)=q1_3(k)*0.0029;
end

%Dextran
files = dir('Flow Transport/Channel 1/Dextran/Jpeg/*.jpg'); %Finds all tif
files in folder
num_files = numel(files); %Finds number of
images
a=imread(files(1).name); %Read in image
mask1=roipoly(a); %Create ROI mask
mask2=roipoly(a);
mask3=roipoly(a);

```

```

close %Close window
for k = 1:num_files %Loop through all
images
a=imread(files(k).name); %Read in image
dF1(k)=mean2(a(mask1)); %Average
intensity of mask on image
dF2(k)=mean2(a(mask2));
dF3(k)=mean2(a(mask3));
q2_1(k)=interp1(cD,conc,dF1(k)); %Concentraion
q2_2(k)=interp1(cD,conc,dF2(k));
q2_3(k)=interp1(cD,conc,dF3(k));
J_dF1(k)=q2_1(k)*0.0029; %Flux
J_dF2(k)=q2_2(k)*0.0029;
J_dF3(k)=q2_3(k)*0.0029;
end

%Static
%Bodipy
files = dir('101211/Bodipy/*.jpg'); %Finds all tif files in folder
num_files2 = numel(files); %Finds number of
images
t2=(0:300:300*(num_files2-1))/3600; %Time between
each image
a=imread(files(1).name); %Read in image
mask1=roipoly(a); %Create ROI mask
mask2=roipoly(a);
mask3=roipoly(a);
close %Close window
k=1;
for k = 1:num_files2 %Loop through
all images
a=imread(files(k).name); %Read in image
bs1(k)=mean2(a(mask1)); %Average
intensity of mask on image
bs2(k)=mean2(a(mask2));
bs3(k)=mean2(a(mask3));
q3_1(k)=interp1(cB,concB,bs1(k)); %Concentraion
q3_2(k)=interp1(cB,concB,bs2(k));
q3_3(k)=interp1(cB,concB,bs3(k));
J_bs1(k)=q3_1(k)*0.023/(max(t2)*3600); %Flux
J_bs2(k)=q3_2(k)*0.023/(max(t2)*3600);
J_bs3(k)=q3_3(k)*0.023/(max(t2)*3600);
end

%Dextran
files = dir('101211/Dextran/*.jpg'); %Finds all tif files in folder
num_files2 = numel(files); %Finds number of
images
a=imread(files(1).name); %Read in image
mask1=roipoly(a); %Create ROI mask
mask2=roipoly(a);
mask3=roipoly(a);
close %Close window
for k = 1:num_files2 %Loop through

```

```

all images
a=imread(files(k).name); %Read in image
dS1(k)=mean2(a(mask1)); %Average
intensity of mask on image
dS2(k)=mean2(a(mask2));
dS3(k)=mean2(a(mask3));
q4_1(k)=interp1(cD,conc,dS1(k)); %Concentraion
q4_2(k)=interp1(cD,conc,dS2(k));
q4_3(k)=interp1(cD,conc,dS3(k));
J_dS1(k)=q4_1(k)*0.023/(max(t2)*3600); %Flux
J_dS2(k)=q4_2(k)*0.023/(max(t2)*3600);
J_dS3(k)=q4_3(k)*0.023/(max(t2)*3600);
end

%Permeability
n=1;
P_bF(n)=0;
P_dF(n)=0;
P_bs(n)=0;
P_ds(n)=0;
for m = 2:num_files
P_bF1(m)=J_bF1(m)/((q1_1(m)-q1_1(n))*S);
P_bF2(m)=J_bF2(m)/((q1_2(m)-q1_2(n))*S);
P_bF3(m)=J_bF3(m)/((q1_3(m)-q1_3(n))*S);
P_bFstd=[P_bF1(m) P_bF2(m) P_bF3(m)];
P_bF(m)=(P_bF1(m)+P_bF2(m)+P_bF3(m))/3;
EbF(m)=std(P_bFstd);
P_dF1(m)=J_dF1(m)/((q2_1(m)-q2_1(n))*S);
P_dF2(m)=J_dF2(m)/((q2_2(m)-q2_2(n))*S);
P_dF3(m)=J_dF3(m)/((q2_3(m)-q2_3(n))*S);
P_dFstd=[P_dF1(m) P_dF2(m) P_dF3(m)];
P_dF(m)=(P_dF1(m)+P_dF2(m)+P_dF3(m))/3;
EdF(m)=std(P_dFstd);
n=m;
end
n=1;
for m = 2:num_files2
P_bs1(m)=J_bs1(m)/((q3_1(m)-q3_1(n))*S);
P_bs2(m)=J_bs2(m)/((q3_2(m)-q3_2(n))*S);
P_bs3(m)=J_bs3(m)/((q3_3(m)-q3_3(n))*S);
P_bsstd=[P_bs1(m) P_bs2(m) P_bs3(m)];
P_bs(m)=(P_bs1(m)+P_bs2(m)+P_bs3(m))/3;
Ebs(m)=std(P_bsstd);
P_ds1(m)=J_ds1(m)/((q4_1(m)-q4_1(n))*S);
P_ds2(m)=J_ds2(m)/((q4_2(m)-q4_2(n))*S);
P_ds3(m)=J_ds3(m)/((q4_3(m)-q4_3(n))*S);
P_dsstd=[P_ds1(m) P_ds2(m) P_ds3(m)];
P_ds(m)=(P_ds1(m)+P_ds2(m)+P_ds3(m))/3;
Eds(m)=std(P_dsstd);
n=m;
end

%Figures
figure()

```

```
errorbar(t1,P_bF,EbF)

figure()
errorbar(t1,P_dF,EdF)

figure()
errorbar(t2,P_bS,EbS)

figure()
errorbar(t2,P_dS,EdS)
```

Cancer migration code to calculate differences between images:

```

clc
clear all
close all

%Channel 1
files = dir('channel1/Channel 1/*.tiff'); %Finds all tif files in folder
num_files = numel(files); %Finds number of images
t1=(0:300:300*(num_files-1))/3600; %Time between each image
j=1; %Set counter to 1
for k = 1:num_files %Loop that goes through all
images
    a=imread(files(k).name); %Reads current image
    b=imread(files(j).name); %Reads previous image
    c=a-b; %Difference in images
    D1(k) = mean2(c); %Find average intensity in
subtracted image
    j=k; %Sets counter to previous image
end

%Channel 3
files3 = dir('channel3/Channel 3/*.tiff'); %Finds all tif files in folder
num_files3 = numel(files3); %Finds number of images
t3=(0:300:300*(num_files3-1))/3600; %Time between each image
l=1; %Set counter to 1
for m = 1:num_files3 %Loop that goes through all
images
    a3=imread(files3(m).name); %Reads current image
    b3=imread(files3(l).name); %Reads previous image
    c3=a3-b3; %Difference in images
    D3(m) = mean2(c3); %Find average intensity in
subtracted image
    l=1; %Sets counter to previous image
end

%Channel 4
files4 = dir('channel4/Channel 4/*.tiff'); %Finds all tif files in folder
num_files4 = numel(files4); %Finds number of images
t4=(0:300:300*(num_files4-1))/3600; %Time between each image
n=1; %Set counter to 1
for o = 1:num_files4 %Loop that goes through all
images
    a4=imread(files4(o).name); %Reads current image
    b4=imread(files4(n).name); %Reads previous image
    c4=a4-b4; %Difference in images
    D4(o) = mean2(c4); %Find average intensity in
subtracted image
    n=1; %Sets counter to previous image
end

%Figure
figure()
plot(t1,D1,t3,D3,t4,D4)
title('Intensity Magnitude of Cell Location Changes')
xlabel('Time (hour)')
ylabel('Average Intensity')
legend('Static', 'Flow 1', 'Flow 2')

```

APPENDIX B

COMSOL SETUP IMAGES

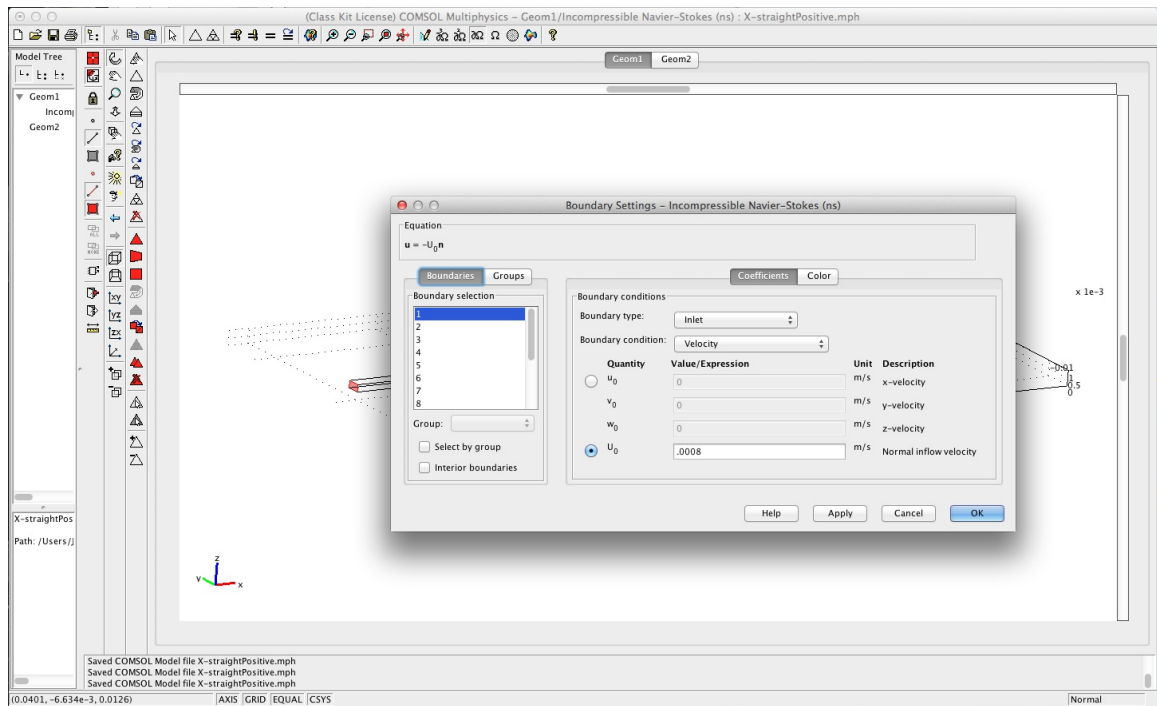


Figure 43: Boundary conditions

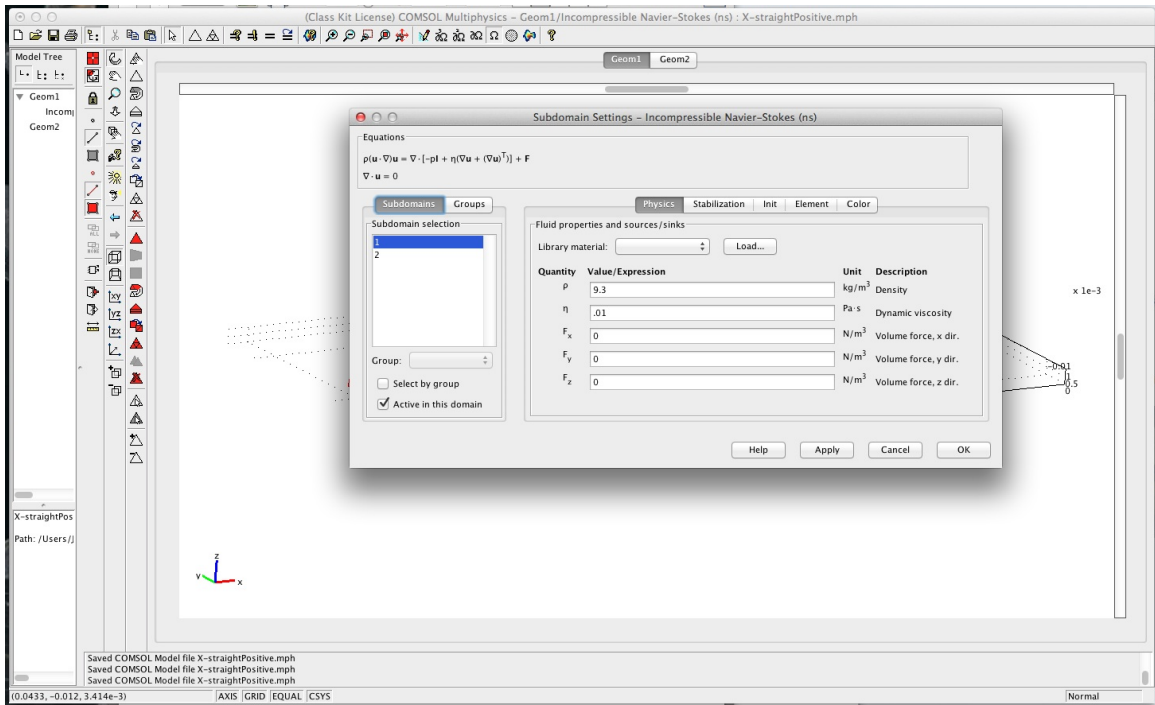


Figure 44: Subdomain conditions

REFERENCES

- [1] With kind permission from Springer Science+Business Media: “Reconstructing organ-level lung function on a chip”, *Science*, vol. 328, 2010, pp. 1662-1668, Dongeun, H., Matthews, B. D., Mammoto, A., Montoya-Zavala, M., Hsin, H. Y., And Ingber, D. E., Figure 1.
- [2] With kind permission from Springer Science+Business Media: “A microfluidic chip for permeability assays of endothelial monolayer”, *Biomed Microdevices*, vol. 12, 2010, pp. 81-88, Shao, J., Wu, L., Wu, J., Zheng, Y., Zhao, H., Lou, X., Jin, Q., and Zhao, J., Figure 1.
- [3] BALUK, P., FUXE, J., HASHIZUME, H., ROMANO, T., LASHNITS, E., BUTZ, S., VESTWEBER, D., CORADA, M., MOLENDINI, C., DEJANA, E., and MCDONALD, D., “Functionally specialized junctions between endothelial cells of lymphatic vessels,” *J Exp Med*, vol. 209, pp. 2349–2362, 2007.
- [4] BATES, D., HILLMAN, N., WILLIAMS, B., NEAL, C., and POCOCK, T., “Regulation of microvascular permeability by vascular endothelial growth factors,” *J Anat*, vol. 200, pp. 581–597, 2002.
- [5] BRAND, C., HUNZIKER, T., and BRAATEHN, L., “Isolation of human skin-derived lymph: flow and output of cells following sodium laurel sulphate-induced contact dermatitis,” *Arch Dermatol Res*, vol. 284, pp. 123–126, 1992.
- [6] CABIOGLU, N., YAZICI, M., ARUN, B., BROGLIO, K., HORTOBAGYI, G., PRICE, J., and SAHIN, A., “Ccr7 and cxcr4 as novel biomarkers predicting axillary lymph node metastasis in t1 breast cancer,” *Clin Cancer Res.*, vol. 11, pp. 5686–5693, 2005.
- [7] CASLEY-SMITH, J., “The influence of tissue hydrostatic pressure and protein concentration on fluid and protein uptake by diaphragmatic initial lymphatics; effect of calcium dobesilate,” *Microcirc Endothelium Lymphatics*, vol. 2, pp. 385–415, 1985.
- [8] CHAMBERS, A., GROOM, A., and MACDONALD, I., “Dissemination and growth of cancer cells in metastatic sites,” *Nat. Rev. Cancer*, vol. 2, pp. 563–572, 2002.
- [9] CLARIJS, R., SCHALKWIJK, L., RUITER, D., and DE WAAL, R., “Lack of lymphangiogenesis despite coexpression of vegf-c and its receptor flt-4 in uveal melanoma,” *Invest. Ophthalmol. Vis. Sci.*, vol. 42, pp. 1422–1428, 2001.
- [10] COGHLIN, C. and MURRAY, G. I., “Current and emerging concepts in tumour metastasis,” *J Pathol*, vol. 222, pp. 1–15, 2010.

- [11] DING, Y., SHIMADA, Y., MAEDA, M., KAWABE, A., KAGANOI, J., KOMOTO, I., HASHIMOTO, Y., MIYAKE, M., HASHIDA, H., and IMAMURA, M., "Association of cc chemokine receptor 7 with lymph node metastasis of esophageal squamous cell carcinoma," *Clin Cancer Res*, vol. 9, pp. 3406–3412, 2003.
- [12] DIXON, J. B., GREINER, S. T., GASHEV, A. A., COTE, G. L., JR, J. E. M., and ZAWIEJA, D. C., "Lymph flow, shear stress, and lymphocyte velocity in rat mesenteric prenodal lymphatics," *Microcirculation*, vol. 13, pp. 597–610, 2006.
- [13] DIXON, J. B., RAGHUNATHAN, S., and SWARTZ, M. A., "A tissue-engineered model of the intestinal lacteal for evaluating lipid transport by lymphatics," *Biotechnology and Bioengineering*, pp. 1–12, 2009.
- [14] DONGEUN, H., MATTHEWS, B. D., MAMMOTO, A., MONTROYA-ZAVALA, M., HSIN, H. Y., and INGBER, D. E., "Reconstructing organ-level lung function on a chip," *Science*, vol. 328, pp. 1662–1668, 2010.
- [15] DRINKER, C., "The functional significance of the lymphatic system: Harvey lecture," *Bull N Y Acad Med*, vol. 14, pp. 231–251, 1938.
- [16] FÖROSTER, R., DAVALOS-MISSLITZ, A., and ROT, A., "Ccr7 and its ligands: balancing immunity and tolerance," *Nat Rev Immunol*, vol. 8, pp. 362–371, 2008.
- [17] GOLDMAN, J., CONLEY, K., RAEHL, A., BONDY, D., PYTOWSKI, B., SWARTZ, M., RUTKOWSKI, J., JAROCH, D., and ONGSTAD, E., "Regulation of lymphatic capillary regeneration by interstitial flow in skin," *Am J Physiol Heart Circ Physiol*, vol. 292, pp. H2176–H2183, 2007.
- [18] GRIFFITH, L. and SWARTZ, M., "Capturing complex 3d tissue physiology in vitro," *Nature Rev Mol Cell Biol*, vol. 7, no. 3, pp. 211–224, 2006.
- [19] GUNTHER, K., LEIER, J., HENNING, G., DIMMLER, A., WEISSBACH, R., HOHENBERGER, W., and FORSTER, R., "Prediction of lymph node metastasis in colorectal carcinoma by expression of chemokine receptor ccr7," *Int J Cancer*, vol. 116, pp. 726–733, 2005.
- [20] HABOLD, C., REICHARDT, F., FOLTZER-JOURDAINNE, C., and LIGNOT, J., "Morphological changes of the rat intestinal lining in relation to body stores depletion during fasting and after refeeding," *Pflugers Arch*, vol. 455, no. 2, pp. 323–332, 2007.
- [21] HARVEY, N., "The link between lymphatic function and adipose biology," *Ann NY Acad Sci*, vol. 1131, no. 1, pp. 82–88, 2008.
- [22] HE, C., YOUNG, A., WEST, C., SU, M., KONERDING, M., and MENTZER, S., "Stimulation of regional lymphatic and blood flow by epicutaneous oxazolone," *J Appl Physiol*, vol. 93, pp. 966–973, 2002.

- [23] HE, Y., RAJANTIE, I., PAJUSOLA, K., JELTSCH, M., HOLOPAINEN, T., YLAHERTTUALA, S., HARDING, T., JOOSS, K., TAKAHASHI, T., and ALITALO, K., "Vascular endothelial cell growth factor receptor 3-mediated activation of lymphatic endothelium is crucial for tumor cell entry and spread via lymphatic vessels," *Cancer Res*, vol. 65, pp. 4739–4746, 2005.
- [24] HELM, C., FLEURY, M., ZISCH, A., BOSCHETTI, F., and SWARTZ, M., "Synergy between interstitial flow and vegf directs capillary morphogenesis in vitro through a gradient amplification mechanism," *Proc Natl Acad Sci USA*, vol. 102, no. 44, pp. 15779–15784, 2005.
- [25] HELM, C., ZISCH, A., and SWARTZ, M., "Engineered blood and lymphatic capillaries in 3-d vegf-fibrin-collagen matrices with interstitial flow," *Biotechnol Bioeng*, vol. 96, no. 1, pp. 167–176, 2007.
- [26] HERESI, G., WANG, J., TAICHMAN, R., CHIRINOS, J., REGALADO, J., LICHTSTEIN, D., and ROSENBLATT, J., "Expression of the chemokine receptor *ccr7* in prostate cancer presenting with generalized lymphadenopathy: Report of a case, review of the literature, and analysis of chemokine receptor expression," *Urol Oncol*, vol. 23, pp. 261–267, 2005.
- [27] HUXLEY, V. H., WILLIAMS, D., JR, D. M., and LAUGHLIN, M., "Altered basal and adenosine-mediated protein flux from coronary arterioles isolated from exercise-trained pigs," *Acta Physiol Scand*, vol. 160, pp. 315–325, 1997.
- [28] HUXLEY, V. H. and SCALLAN, J., "Lymphatic fluid: exchange mechanisms and regulation," *J Physiol*, vol. 589, no. 12, pp. 2935–2943, 2011.
- [29] ITANO, A. A. and JENKINS, M., "Antigen presentation to native cd4 t cells in the lymph node," *Nature Immunol*, vol. 4, pp. 733–739, 2003.
- [30] JI, R., "Lymphatic endothelial cells, tumor lymphangiogenesis and metastasis: New insights into intratumoral and peritumoral lymphatics," *Cancer Metastasis Rev*, vol. 25, pp. 677–694, 2006.
- [31] KITAYAMA, J., TABUCHI, M., TSURITA, G., ISHIKAWA, M., OTANI, K., and NAGAWA, H., "Adiposity and gastrointestinal malignancy," *Digestion*, vol. 79, pp. 26–32, 2009.
- [32] LEAK, L. and BURKE, J., "Ultrastructural studies on the lymphatic anchoring filaments," *J Cell Biol*, vol. 36, pp. 129–149, 1968.
- [33] LIU, J., HSU, W.-J., PARSA, H., DAS, A., ROUSE, R., and SIA, S. K., "Real-time microfluidic system for studying mammalian cells in 3d microenvironments," *Am J Physiol Heart Circ*, vol. 80, no. 10, p. 36403647, 2008.
- [34] MANDRIOTA, S., JUSSILA, L., JELTSCH, M., COMPAGNI, A., BAETENS, D., PREVO, R., BANERJI, S., HUARTE, J., MONTESANO, R., JACKSON, D., and

- ET AL, "Vascular endothelial growth factor-c-mediated lymphangiogenesis promotes tumor metastasis," *EMBO J*, vol. 20, pp. 672–682, 2001.
- [35] MASHINO, K., SADANGA, N., YAMAGUCHI, H., TANKA, F., OHTA, M., SHIBUTA, K., INOUE, H., and MORI, M., "Expression of chemokine receptor *ccr7* is associated with lymph node metastasis of gastric carcinoma," *Cancer Res*, vol. 62, pp. 2937–2941, 2002.
- [36] MEBIUS, R., STREETER, P., BREVE, J., DUIJVESTIJN, A., and KRAAL, G., "The influence of afferent lymphatic vessel interruption on vascular addressing expression," *J Cell Biol*, vol. 115, pp. 85–95, 1991.
- [37] MITEVA, D. O., RUTKOWSKI, J. M., DIXON, J. B., KILARSKI, W., SHIELDS, J. D., and SWARTZ, M. A., "Transmural flow modulates cell and fluid transport functions of lymphatic endothelium," *Circ Res*, vol. 106, pp. 920–931, 2010.
- [38] MULLINS, R. and HUDGENS, R., "Increased skin lymph protein clearance after 6-h arterial bradykinin infusion," *AM J Physiol*, vol. 253, pp. H1462–H1469, 1987.
- [39] NATHANSON, S., "Insights into the mechanisms of lymph node metastasis," *Cancer*, vol. 98, pp. 413–423, 2003.
- [40] OLSZEWSKI, W., ENGESET, A., ROMANIUK, A., GRZELAK, I., and ZIOLKOWSKA, A., "Immune cells in peripheral lymph and skin of patients with obstructive lymphedema," *Lymphology*, vol. 23, pp. 23–33, 1990.
- [41] PAPE, K., CATRON, D., ITANO, A., and JENKINS, M., "The humoral immune response is initiated in lymph nodes by b cells that acquire soluble antigen directly in the follicles," *Immunity*, vol. 26, pp. 491–502, 2007.
- [42] PORTER, C. J. H. and ET AL., "Lipids and lipid-based formulations: Optimizing the oral delivery of lipophilic drugs," *Nature Reviews Drug Discovery*, vol. 6, pp. 231–248, 2007.
- [43] RANDOLPH, G., ANGELI, V., and SWARTZ, M., "Dendritic-cell trafficking to lymph nodes through lymphatic vessels," *Nat Rev Immunol*, vol. 5, pp. 617–628, 2005.
- [44] ROCKSON, S., "The elusive adipose connection," *Lymphatic Res Biol*, vol. 2, no. 3, pp. 105–106, 2004.
- [45] ROSEN, E., "The molecular control of adipogenesis, with special reference to lymphatic pathology," *Ann NY Acad Sci*, vol. 979, pp. 143–158, 2002.
- [46] RUTKOWSKI, J., BOARDMAN, K., and SWARTZ, M., "Characterization of lymphangiogenesis in a model of adult skin regeneration," *Am J Physiol Heart Circ Physiol*, vol. 291, pp. H1402–H1410, 2006.

- [47] RUTKOWSKI, J., MOYA, M., JOHANNES, J., GOLDMAN, J., and SWARTZ, M., “Secondary lymphedema in mouse tail: lymphatic hyperplasia, vegf-c up regulation, and the protective role of mmp-9,” *Microvasc Res*, vol. 72, no. 3, pp. 161–171, 2006.
- [48] RYAN, T., “Adipose tissue and lymphatic function: Is there more to this story especially for tropical diseases?,” *Lymphology*, vol. 39, no. 1, pp. 49–52, 2006.
- [49] SCHMID-SCHÖNBEIN, G., “Microlymphatics and lymph flow,” *Physiol Rev*, vol. 70, no. 4, pp. 987–1028, 1990.
- [50] SCHMID-SCHÖNBEIN, G., “The second valve system in lymphatics,” *Lymphat Res Biol*, vol. 1, pp. 25–29, 2003.
- [51] SHAO, J., WU, L., WU, J., ZHENG, Y., ZHAO, H., LOU, X., JIN, Q., and ZHAO, J., “A microfluidic chip for permeability assays of endothelial monolayer,” *Biomed Microdevices*, vol. 12, pp. 81–88, 2010.
- [52] SHIELDS, J., FLEURY, M., YONG, C., TOMEL, A. A., RANDOLPH, G., and SWARTZ, M., “Autologous chemotaxis as a mechanism of tumor cell homing to lymphatics via interstitial flow and autocrine ccr7 signaling,” *Cancer Cell*, vol. 11, pp. 526–538, 2007.
- [53] SIPOS, B., KOJIMA, M., TIEMANN, K., KLAPPER, W., DRUSE, M., KALTHOFF, H., SCHNIEWIND, B., TEPEL, J., WEICH, H., KERJASCHKI, D., and KLOPPPEL, G., “Lymphatic spread of ductal pancreatic adenocarcinoma is independent of lymphangiogenesis,” *J Pathol*, vol. 207, pp. 301–312, 2005.
- [54] STACKER, S., CAESAR, C., BALDWIN, M., THORNTON, G., WILLIAMS, R., PREVO, R., JACKSON, D., NISHIKAWA, S., KUBO, H., and ACHEN, M., “Vegf-d promotes the metastatic spread of tumor cells via the lymphatics,” *Nat Med*, vol. 7, pp. 186–189, 2001.
- [55] TAKANAMI, I., “Overexpression of ccr7 mrna in non small cell lung cancer: Correlation with lymph node metastasis,” *Int J Cancer*, vol. 105, pp. 186–189, 2003.
- [56] TAKEUCHI, H., FUJIMOTO, A., TANAKA, M., YAMANO, T., HSUEH, E., and HOON, D., “Ccl21 chemokine regulates chemokine receptor ccr7 bearing malignant melanoma cells,” *Clin Cancer Res*, vol. 10, pp. 2351–2358, 2004.
- [57] TOBLER, N. and DETMAR, M., “Tumor and lymph node lymphangiogenesis-impact on cancer metastasis,” *J Leukoc Biol*, vol. 80, pp. 691–696, 2006.
- [58] TRZEWIK, J., MALLIPATTU, S., ARTMANN, G., DELANO, F., and SCHMID-SCHÖNBEIN, G., “Evidence for a second valve system in lymphatics: endothelial microvalves,” *FASEB J*, vol. 15, pp. 1711–1717, 2001.

- [59] TSO, P. and BALINT, J., “Formation and transport of chylomicrons by enterocytes to the lymphatics,” *Am J Physiol*, vol. 250, pp. G715–G726, 1986.
- [60] TSO, P., PITTS, V., and GRANGER, D., “Role of lymph flow in intestinal chylomicron transport,” *Am J Physiol*, vol. 249, no. 1, pp. G21–G28, 1985.
- [61] VAN DER MEER, A., VERMEUL, K., POOT, A., FEIJEN, J., and VERMES, I., “A microfluidic wound-healing assay for quantifying endothelial cell migration,” *Am J Physiol Heart Circ*, vol. 298, pp. H719–H725, 2010.
- [62] WANG, J., ZHANG, X., THOMAS, S., GRANDIS, J., WELLS, A., CHEN, Z., and FERRIS, R., “Chemokine receptor 7 activates phosphoinositide-3 kinase-mediated invasive and pro survival pathways in head and neck cancer cells independent of egfr,” *Oncogene*, vol. 24, pp. 5897–5904, 2005.
- [63] WILEY, H., GONZALES, E., MAKI, W., WU, M., and HWANG, S., “Expression of cc chemokine receptor-7 and regional lymph node metastasis of b16 murine melanoma,” *J P Natl Cancer Inst*, vol. 93, pp. 1638–1643, 2001.
- [64] WILLIAMS, C., LEEK, R., ROBSON, A., BANERJI, S., PREVO, R., HARRIS, A., and JACKSON, D., “Absence of lymphangiogenesis and intratumoural lymph vessels in human metazoic breast cancer,” *J Pathol*, vol. 200, pp. 195–206, 2003.
- [65] WITTE, M., JONES, K., WILTING, J., DICTOR, M., SELG, M., MCHALE, N., GERSHENWALD, J., and JACKSON, D., “Structure function relationships in the lymphatic system and implications for cancer biology,” *Cancer Metastasis Rev*, vol. 25, pp. 159–184, 2006.
- [66] WONG, S., HAACK, H., CROWLEY, D., BARRY, M., BRONSON, R., and HYNES, R., “Tumor-secreted vascular endothelial growth factor-c is necessary for prostate cancer lymphangiogenesis, but lymphangiogenesis is unnecessary for lymph node metastasis,” *Cancer Res*, vol. 65, pp. 9789–9798, 2005.